The Orbital Architecture and Debris Disks of the HR 8799 Planetary System

Krzysztof Goździewski and Cezary Migaszewski
Faculty of Physics, Astronomy and Informatics, Nicolaus Copernicus University, Grudziądzka 5, 87-100 Toruń, Poland

Abstract

The HR 8799 planetary system with four $\simeq 10\,m_{\rm Jup}$ planets in wide orbits up to $\simeq 70$ au and orbital periods up to 500 yr has been detected with direct imaging. Its intriguing orbital architecture is not yet fully resolved due to time-limited astrometry covering only $\simeq 20$ yr. Earlier, we constructed a heuristic model of the system based on rapid, convergent migration of the planets. Here we develop a better-structured and CPU-efficient variant of this model. With the updated approach, we reanalyzed the self-consistent, homogeneous astrometric data set in Konopacky et al. The best-fitting configuration agrees with our earlier findings. The HR 8799 planets are likely involved in a dynamically robust Laplace 8e:4d:2c:1b resonance chain. Hypothetical planets with masses below the current detection limit of 0.1–3 $m_{\rm Jup}$ within the observed inner or beyond the outer orbit, respectively, do not influence the long-term stability of the system. We predict the positions of such nondetected objects. The long-term stable orbital model of the observed planets helps to simulate the dynamical structure of debris disks in the system. A CPU-efficient fast indicator technique makes it possible to reveal their complex, resonant shape in 10^6 particles scale. We examine the inner edge of the outer disk detected between 90 and 145 au. We also reconstruct the outer disk, assuming that it has been influenced by the convergent migration of the planets. A complex shape of the disk strongly depends on various dynamical factors, like orbits and masses of nondetected planets. It may be highly noncircular, and its models are yet nonunique regarding both observational constraints and its origin.

Key words: astrometry – celestial mechanics – methods: numerical – planets and satellites: dynamical evolution and stability – stars: individual (HR 8799)

1. Introduction

The HR 8799 planetary system was discovered by Marois et al. (2008) as a three-planet configuration. After 2 yr, the fourth innermost planet was announced by the same team (Marois et al. 2010). Since the discovery, this unusual extrasolar planetary system has been studied in literally tens of papers. The parent-star age and companion masses, as well as the orbital architecture and its long-term stability, debris disks, and formation, are analyzed in, e.g., Goździewski & Migaszewski (2009), (2014); Lafrenière et al. (2009); Metchev et al. (2009); Reidemeister et al. (2009); Su et al. (2009); Fabrycky & Murray-Clay (2010); Hinz et al. (2010); Marshall et al. (2010); Moro-Martín et al. (2010); Bergfors et al. (2011); Currie et al. (2011), (2012); Galicher et al. (2011); Soummer et al. (2011); Baines et al. (2012); Sudol & Haghighipour (2012); Esposito et al. (2013); Oppenheimer et al. (2013); Marleau & Cumming (2014); Matthews et al. (2014); Maire et al. (2015); Pueyo et al. (2015); Booth et al. (2016); Contro et al. (2016); Currie (2016); Götberg et al. (2016); Konopacky et al. (2016); Zurlo et al. (2016); Wertz et al. (2017); Read et al. (2018); Wilner et al. (2018); and counting.

Regarding a characterization of the parent star and its planets, as well as the past and to-date observations of debris disks in the system, we refer to the recent papers by Booth et al. (2016), Read et al. (2018), and Wilner et al. (2018) and references therein. Following these works, the star is very young, ~60 Myr, within the most likely interval of 30–160 Myr. We adopt its mass $m_\star$ of $1.52\,M_\odot$ and masses of the planets in the range of 5–10 $m_{\rm Jup}$ (Marois et al. 2010).

In spite of the enormous literature on the HR 8799 system, many questions are still open. The global, orbital structure of the HR 8799 system is a particularly interesting problem. The ratio of $\simeq 120$ (α, δ) measurements in the literature, collected in Wertz et al. (2017), to 24 geometrical elements (free parameters) is 4–5,

and it did not significantly change over the past few years, since the discovery of the fourth companion in Marois et al. (2010). Moreover, the major limitation of the astrometric models is small coverage of the orbits by the measurements, between $\simeq 3\%$ and $\simeq 12\%$ for planets HR 8799b and HR 8799e, respectively, given significant uncertainties of $\simeq 10$ mas. These weak observational constraints permit a variety of nonunique orbital geometries, although all of them seem to be equally good fits to the observations (e.g., Konopacky et al. 2016; Wertz et al. 2017).

A dynamical analysis of the best-fitting Keplerian solutions reveals that they represent crossing orbits and configurations that are unstable in an enormously short 0.5–1 Myr timescale. Simple and natural requirements of the stability, like the Hill criterion, do not constrain the orbital models either, e.g., Konopacky et al. (2016, their Figure 3) and Wertz et al. (2017, their Figure B.1, especially the panel for planet d). Finding long-term stable configurations simultaneously fulfilling astrometric and mass constraints is difficult even for the lower limit of the star age of 30 Myr and the low limit of the planet masses.

It is still uncertain whether or not the system is strongly resonant, long-term or only marginally stable, or unstable at all (e.g., Goździewski & Migaszewski 2009, 2014; Fabrycky & Murray-Clay 2010; Götberg et al. 2016). It may remain a matter of some philosophical debate unless the orbits are observationally sampled for a sufficiently long interval of time. Furthermore, it is unclear how the system was formed (Marois et al. 2010), given that massive planetary or brown-dwarf companions are found relatively close to the star.

Regarding dynamical arguments, none of analytic or semi-analytic criteria of stability apply to the HR 8799 system. The early dynamical studies of the three-planet system (Marois et al. 2008; Goździewski & Migaszewski 2009; Reidemeister et al. 2009; Fabrycky & Murray-Clay 2010) revealed that even quasi-circular and apparently wide $\simeq 70$ au orbits are separated

by less than 3–4 mutual Hill radii. Such configurations are predicted as self-destructing statistically in a fraction of a 1 Myr timescale (Chambers et al. 1996; Chatterjee et al. 2008; Morrison & Kratter 2016) unless a protecting dynamical mechanism is present. Indeed, coplanar or close to coplanar orbits of three outer planets involved in a stable Laplace 4d:2c:1b mean-motion resonance (MMR) were found, explaining the astrometric observations of the HR 8799 system, shortly after its discovery (Goździewski & Migaszewski 2009; Reidemeister et al. 2009; Fabrycky & Murray-Clay 2010; Marshall et al. 2010; Soummer et al. 2011).

However, the stability problem became much harder with the fourth planet announced in Marois et al. (2010). Even assuming a protecting MMR mechanism, the orbital parameters of long-living configurations may vary only within small limits (Goździewski & Migaszewski 2014) or must be particularly tuned, since they are extremely chaotic and prone to tiny changes of the initial conditions and the numerical integrator scheme (Götberg et al. 2016).

Seeking long-term stable orbits of the planets has a "practical" aspect, since they are needed for simulating debris disks in the system (Booth et al. 2016; Contro et al. 2016; Read et al. 2018; Wilner et al. 2018). The outer debris disk might be present between $\simeq 90$ and $\simeq 450$ au. According to models of the ALMA observations in Booth et al. (2016) and Read et al. (2018), the inner edge of this disk should be placed at ~ 145 au, beyond the direct influence attributed to planet HR 8799b at roughly ~ 90 au. It might indicate the presence of an additional fifth planet below the current detection limit of a few Jupiter masses. However, Wilner et al. (2018) argued that combined ALMA and VLA observations with higher spatial resolution do not favor the fifth-planet hypothesis, and the inner border of the disk may be detected at $\simeq 104$ au, consistent with the currently known four-planet configuration. Moreover, they constrained the outermost planet mass $m_b \simeq 6^{+7}_{-3}\, m_{\rm Jup}$.

We note that some of the works devoted to debris disks (Booth et al. 2016; Contro et al. 2016; Read et al. 2018) made use of our best-fitting model representing the Laplace MMR chain (Goździewski & Migaszewski 2014), which was found with observations up to the epoch of 2013. The most recent papers regarding the astrometric models of the HR 8799 system based on to-date observations, until epoch 2014.93, focus mostly on Keplerian solutions (Konopacky et al. 2016; Wertz et al. 2017). These best-fitting, or most likely, models, in terms of the Bayesian inference, exhibit different geometries, such as non-coplanar, highly eccentric nonresonant, or partly resonant orbits, but have not been examined for their long-term orbital stability. Therefore, such solutions are not suitable for the dynamical analysis of the debris disks.

In this work, we propose to resolve the structure of these disks with CPU-efficient fast indicators based on the maximal Lyapunov characteristic exponent (mLCE), instead of integrating orbits for a required full time span. For that purpose, we need to construct long-term, rigorously stable orbits of the planets that are robust against small perturbations. Such stable planetary models are helpful to localize "missing" (nondetected) planets or to investigate influence of such putative planets on the debris disks.

This paper is structured as follows. After this Introduction, Section 2 presents an update of the model of astrometric data through constraining it by the process of planetary migration.

Section 3 regards the results and details of orbital architectures of the HR 8799 system derived for a self-consistent set of astrometric measurements in Konopacky et al. (2016) made with the Keck II telescope. The results in this part support our idea of the orbital analysis or could be at least an alternative and reasonable approach when compared with other solutions in the literature. Section 4 is for our model of debris disks based on the fast indicator technique, and we describe the results of its time calibration with the direct numerical integrations. Simulations of yet-undetected planets in the system are described in Sections 5 and 6. We analyze the dynamical structure of the inner and outer debris disks in Sections 5 and 7, respectively. We also investigate a scenario of the outer disk influenced by migrating planets in Section 8. Some apparent discrepancies between our approach and the results in the recent literature are addressed in Section 9. We summarize the work in Section 10.

2. The Migration Algorithm Revisited

The phase space of mutually interacting planetary systems has a discrete, noncontinuous structure (Malhotra 1998). This feature may be useful to introduce implicit constraints on the otherwise huge multidimensional space of free parameters. The key idea relies on the evolution of the orbital elements in migrating planetary systems. Due to the planetary migration, these elements may be tightly self-constrained, depending on an established MMR. We assume that such, although not necessarily a realistic or fully resolved dynamical process, orders the planetary system and drives it to an equilibrium state. In such a state, the orbital elements, like the semimajor axes, orbital phases, and eccentricities, are limited to certain narrow ranges. This coherence is crucial, since it also provides the long-term dynamical stability.

The essential optimization problem is to find MMR-trapped systems that reproduce the observations at some time. We solved it with the migration constrained optimization algorithm (MCOA), as dubbed earlier in Goździewski & Migaszewski (2014). The MCOA makes use of a heuristic model of the planetary migration (Beaugé et al. 2006; Moore et al. 2013) and theoretical estimates of the planetary masses, consistent with the recent cooling theory (Marois et al. 2010; Baines et al. 2012; Marleau & Cumming 2014).

The original MCOA would require repeating CPU-demanding computations if the astrometric data significantly change. A recent publication of revised and unified astrometric measurements in Konopacky et al. (2016) inspired us to search for CPU-efficient, and perhaps improved, implementations of the method. Indeed, we developed a better-structured computational strategy that consists of two essentially independent steps. These steps may be conducted individually, instead of running the original monolithic code. The updated scheme, much easier to follow and repeat, if necessary, is illustrated in Figure 1 and described below. (Figure 1 may be considered a graphical plan of this paper.)

2.1. A Set of MMR-captured Systems

At the first step, we build a database of systems formed through migration of an appropriate number of planets. Their semimajor axes may be only roughly consistent with the observations. We consider coplanar systems, following arguments behind the
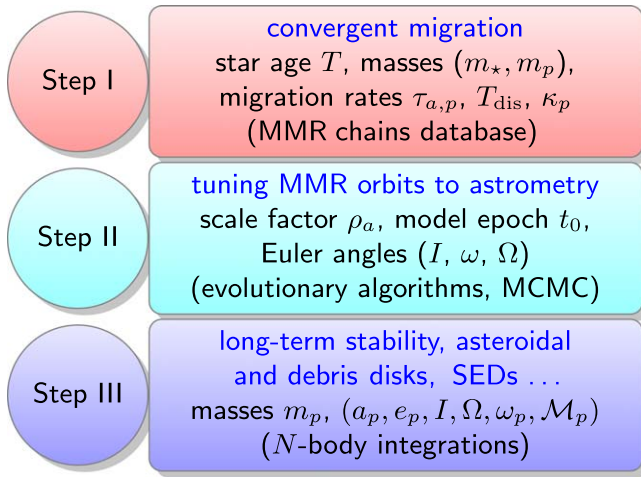
Step I — convergent migration
star age T, masses $(m_\star, m_p)$,
migration rates $\tau_{a,p}$, $T_{\rm dis}$, κ_p
(MMR chains database)

Step II — tuning MMR orbits to astrometry
scale factor ρ_a, model epoch t_0,
Euler angles (I, ω, Ω)
(evolutionary algorithms, MCMC)

Step III — long-term stability, asteroidal
and debris disks, SEDs . . .
masses m_p, $(a_p, e_p, I, \Omega, \omega_p, \mathcal{M}_p)$
(N-body integrations)

Figure 1. Graphical representation of the MCOA. Major steps and the most important parameters are listed. The diagram also illustrates a plan of this work. See the text for details.

planetary migration theory (e.g., Armitage 2018 and references therein). Orbital elements such as eccentricity, nodal angle, and mean anomaly are self-consistently tuned by the migration. The planetary masses may be constrained by cooling models (Baraffe et al. 2003; Marleau & Cumming 2014) or sampled from a preselected distribution.

We may consider any reasonable variant of the migration theory at this stage. The crucial point is that the planetary migration leads to the MMR capture and establishes stable systems. In order to mimic the migration with the N-body code, we modify the astrocentric equations of motion with a force term (Beaugé et al. 2006; Papaloizou & Terquem 2006; Moore et al. 2013),

$$\boldsymbol{f}_i = -\frac{\boldsymbol{v}_i}{2\tau_i} - \frac{\boldsymbol{v}_i - \boldsymbol{v}_{c,i}}{\kappa_i^{-1}\tau_i}, \qquad (1)$$

where $\boldsymbol{v}_i$ is the astrocentric velocity of planet $i = 1, 2, 3, \ldots, N$, and $\boldsymbol{v}_{c,i}$ is a velocity of planet i at a circular Keplerian orbit at the distance of this planet. We note that the HR 8799 planets are numbered with $i = 1, 2, 3, \ldots$ with respect to their increasing distance from the star, or we mark them with Roman letters, from the innermost "e" $\equiv$ "1" to the outermost "4" $\equiv$ "b" or "f" $\equiv$ "5," following the order in which they were discovered and named (Marois et al. 2008, 2010).

The timescale of migration of planet i is denoted with τ_i, while κ_i is the ratio between τ_i and the timescale of orbital circularization, which may be uniform for all planets in the system. Moreover, τ_i could depend on time that simulates a dispersal of the disk, i.e., $\tau_i = \tau_i(t = 0)\exp(t/T_{\rm dis})$, where $T_{\rm dis}$ is the characteristic time of the decay.

The migration experiments described below were conducted with the initial semimajor axes by 3–4 times as large as in the observed system, yet each one was selected randomly within a 50% deviation from its nominal values for the 8e:4d:2c:1b Laplace resonance. The initial eccentricities were selected randomly, $e_{1,2,3,4} \in [0, 0.16)$. The pericenter arguments ϖ_i and the mean anomalies $\mathcal{M}_i$ were drawn from the uniform distribution in $[0°, 360°)$. As for the planetary masses m_i, we choose the uniform distribution limited within the $[6, 10]$ $m_{\rm Jup}$ range.

In order to introduce a variability in the outcome configurations, we considered a few variants of Equation (1), with κ_i selected randomly for each planet around a mean $\kappa \in [1, 300)$ or by choosing it the same for all planets. We also randomly changed the dispersal time $T_{\rm dis} \in [1, 30]$ Myr, or it was infinite. We randomized individual timescales of the migration $\tau_i \in [1, 30]$ Myr, forming a decreased sequence, in order to obtain convergent migration.

The equations of motion were integrated until a traced system did not disrupt and the hierarchy of the initial semimajor axes was preserved. We stopped the integrations when the inner semimajor axis in the migrating systems became $a_1 < 14.6$ au. Then we integrated the N-body equations of motion without dissipation for an additional 32,768 steps of 400 days ($\sim 1/45$ of the innermost period), in order to determine the proper mean motions for all planets. The proper mean motions are the fundamental frequencies f_i resolved with the refined Fourier frequency analysis (Laskar 1993; Šidlichovský & Nesvorný 1996) of the time series $\{a_i(t)\exp(i\lambda_i(t))\}$, where $a_i(t)$ and $\lambda_i(t)$ are the canonical osculating semimajor axis and the mean longitude, respectively, as inferred in the Jacobi or Poincaré frame. Then we computed the linear combinations of the fundamental frequencies,

$$\Delta f(\boldsymbol{n}) \equiv \sum_{i=1}^{N} n_i f_i,$$

where $\boldsymbol{n} \equiv [n_1, \ldots, n_N]$ is a vector of integers in the $[-6, 6]$ range, which yields small $|\Delta f|$. In this way, we aimed to find possible low-order multibody MMR chains. Simultaneously, we examined critical angles corresponding to $\boldsymbol{\eta} = \arg\min|\Delta f(\boldsymbol{n})|$,

$$\theta_{\boldsymbol{\eta}}(t) \equiv \sum_{i=1}^{N} \eta_i \lambda_i.$$

If $|\boldsymbol{\eta}| = 0$, in accord with the d'Alambert rule, then the resonant configuration may be called the generalized Laplace resonance (Papaloizou 2015), or the multiple MMR chain of zeroth order.

Two typical examples of the resonance capture of four-planet systems are illustrated in Figure 2. The left column is for a system trapped in the generalized Laplace resonance that exhibits librations of at least two critical angles, with amplitudes of several degrees: the "classic" Laplace resonance, which we studied in Goździewski & Migaszewski (2014), is distinguished through

$$\theta_{8:4:2:1} \equiv \theta_{1:-2:-1:2} = \lambda_1 - 2\lambda_2 - \lambda_3 + 2\lambda_4,$$

as well as another critical angle $\theta_{-1:4,-5:2}$. In this four-body MMR chain, the orbital period ratios are pairwise close to 2.

The second example, in the right column of Figure 2, shows a zeroth-order four-body MMR with librations of only one critical angle $\theta_{-1,4,-6,3}$ ($\theta_{8:4:2:1}$ circulates). Moreover, the middle pair of planets exhibits the orbital period ratio close to 2:5 (see the bottom panel with Δf in Figure 2).

In both cases, the inner eccentricities are excited to moderate values of $\simeq 0.1$, which usually leads to good orbital fits.

Figure 3 shows the distribution of osculating astrocentric orbital periods and eccentricities attained when $a_1 < 14.6$ au. At this moment, which is the reference zero epoch for further optimization, the migration simulation was stopped. A feature
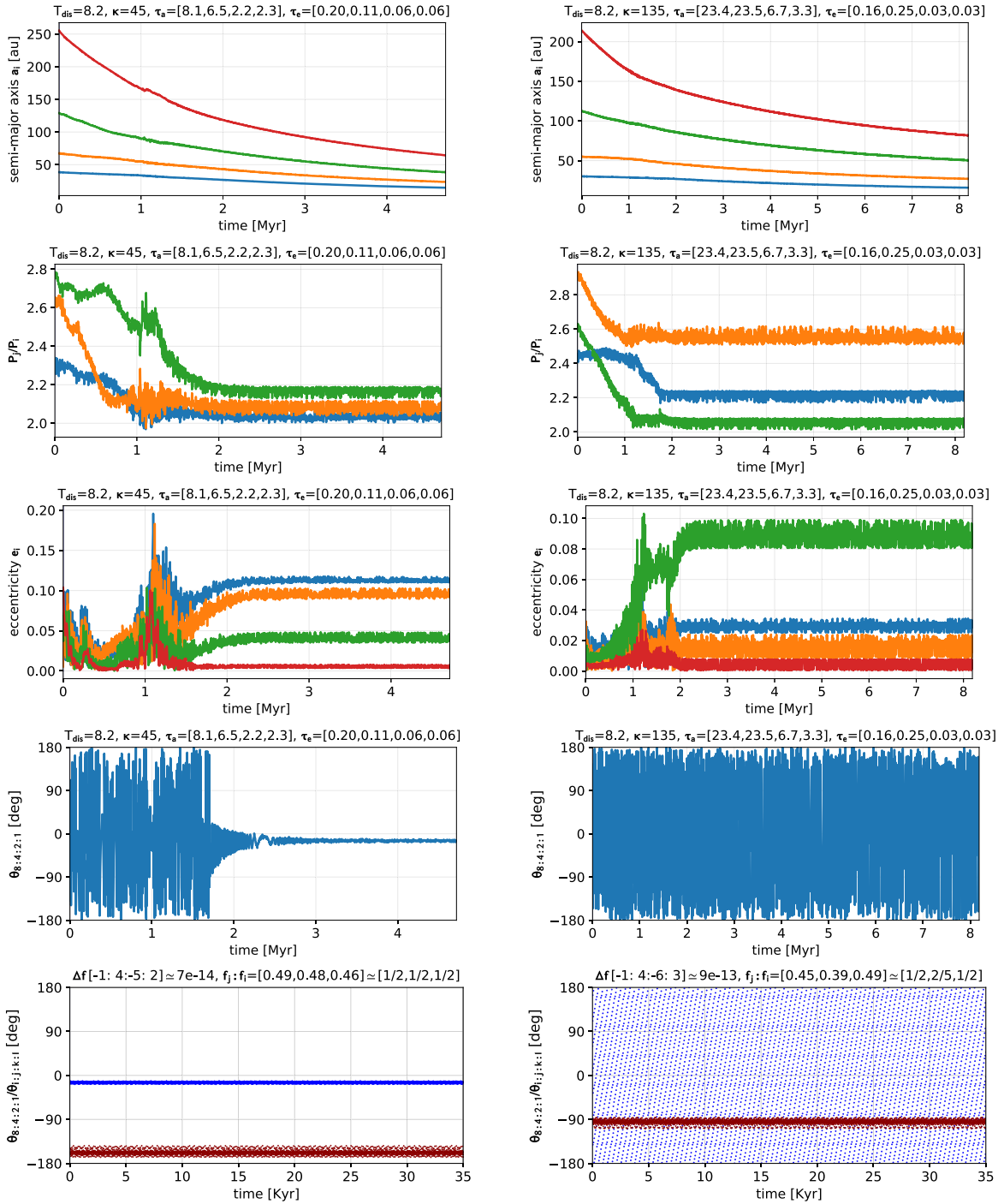
Figure 2. Migration capture of four HR 8799 planets into the generalized Laplace resonances. Panels from top to bottom illustrate temporal evolution of the semimajor axes, orbital period ratios of subsequent pairs of planets, eccentricities, and the critical arguments (two bottom panels). The disk decay timescale $T_{\rm dis}$, as well the migration timescales $\tau_{\rm a}$ and $\tau_{\rm e} \equiv \kappa^{-1}\,\tau_{\rm a}$ in square brackets, are in Myr; $P_{j:Pi}$ and $f_j:f_i$ mean ratios of the astrocentric orbital periods and the proper mean motions f_i for subsequent pairs of planets; $\Delta f[\eta_1, \eta_2, \eta_3, \eta_4]$ is for the absolute range of the linear combination of the frequencies f_i and is expressed in radians per the so-called long day of $2\pi\,{\rm yr}^{-1} \simeq 58.13$ days. All panels were generated in the course of the simulations. See the text for more details.

of this distribution is an overpopulated regime of 2:1 MMR for subsequent pairs of planets. The 2:1 MMR appears most "easily," in spite of significantly varied initial orbits, masses, and migration parameters. The final eccentricities may be as large as 0.2, yet the most frequent values are found around 0.02–0.05.

The statistics of migrated configurations illustrated in Figure 3 also involves a significant fraction of systems with

the innermost and outermost pairs in the 3:1 MMR. However, such systems do not fit the observations, since the semimajor axis of HR 8799b appears to be too wide, $a_{\rm b} \sim 80$ au.

An interesting result flowing from identification of the MMRs is a dominant proportion of the zeroth-order MMR chains, which may be estimated to be as large as ~90% in the total sample of $\sim 1.5 \times 10^5$ systems. It may deserve further study, which we aim to conduct in a separate work.
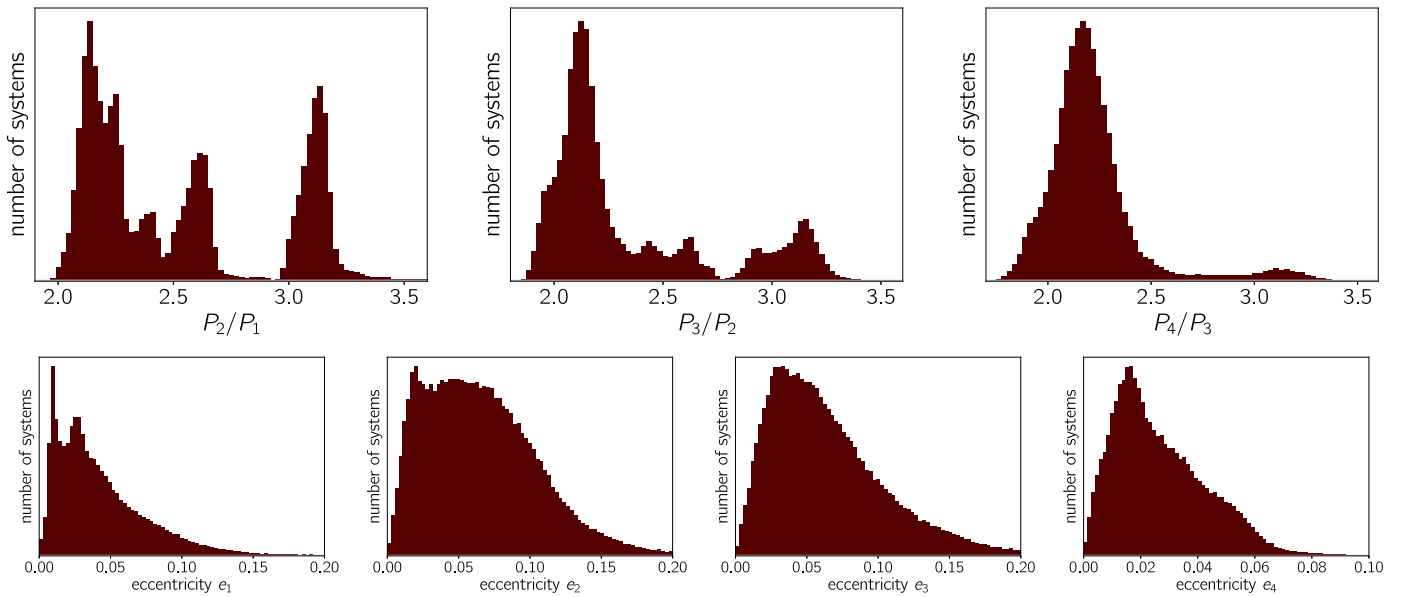
Figure 3. Graphical representation of the MCOA database that consists of $\sim 1.5 \times 10^5$ four-planet configurations obtained through the planetary migration. The top row is for the distribution of osculating, astrocentric period ratios at the epoch zero, when the inner semimajor axis $a_e < 14.6$ au. Peaks in the top row indicate low-order two-body MMRs. The bottom row is for the distribution of osculating, astrocentric eccentricities at the zero epoch.

Similar results were obtained at early preparation of this paper regarding five-planet systems, with a hypothetical planet HR 8799f beyond the orbit of HR 8799b and a small mass of $\simeq 2\,m_{\rm Jup}$ below the present detection level. In this case, the initial spread of semimajor axes in migrating systems was closer ($\pm 20\%$) to the 2:1 MMRs for subsequent pairs. Regarding eccentricity, the only qualitative difference with the four-planet simulations is a longer tail in the histogram for planet b, extended for $e_{\rm b} \sim 0.15$, which is forced by the outer planet HR 8799f.

Here we consider essentially the most simple model of the migration. One could apply more sophisticated theories accounting for the mass growth or stochastic migration (Papaloizou & Terquem 2006; Armitage 2018). At this stage, it is more important to gather a large set of orbital elements representing long-term stable systems, trapped in possibly different MMRs, than to analyze the process in fully realistic settings.

2.2. Constraining MMR Orbits with Astrometric Data

At the next step, the MMR-trapped systems from the MCOA database are fine-tuned to fit particular or all available observations. Only a fraction of them may reproduce the observed system. Here we rely on the scale-free property of the N-body equations of motion, which allows for scaling the semimajor axes through a factor of $\rho_{\rm a} > 0$, without changing the dynamical character of the scaled system.

We find the osculating epoch $t_0 \in [-T_0, T_0]$, relative to the end time of the migration (zero epoch), where T_0 is typically $\sim 10^3$ outermost periods, since the orbits have different orbital periods and quickly precess ($\varpi \simeq -500'' \,{\rm yr}^{-1}$). We also need to fit three Euler angles (I, Ω, ω) that rotate the orbital plane of the original system to the observer (sky) plane. The synthetic astrocentric signal is derived by propagating linearly rescaled orbits through the numerical solution of the N-body equations of motion for time t_0, relative to the zero epoch of the migration, with the initial eccentricities and orbital phases of

their self-consistent, MMR-fixed values. The parameters $\boldsymbol{p} = (\rho_{\rm a}, t_0, I, \Omega, \omega)$ are arguments of the merit function expressed as $\chi_\nu^2(\boldsymbol{p})$ or the maximum-likelihood function $\log \mathcal{L}(\boldsymbol{p}) \sim -\chi_\nu^2(\boldsymbol{p})/2$ (Bevington & Robinson 2003). We use the Bulirsh–Stoer–Gragg (BSG) numerical integrator to solve the equations of motion (Hairer et al. 2002). The absolute and relative local error limits are set to $\sim 10^{-15}$.

We underline that the astrocentric model of the observations is based on the self-consistent canonical N-body dynamics, unlike the Keplerian geometric parameterization used frequently in the literature. The N-body model is more CPU-demanding, but it explicitly accounts for the planetary masses and the mutual gravitational interactions between the planets. We demonstrate its importance when discussing the results (Section 3).

The optimization is performed for a number of MMR systems with the help of evolutionary algorithms (Charbonneau 1995; Price et al. 2005; Izzo et al. 2012). Furthermore, the Bayesian inference and MCMC sampling make it possible to introduce prior information on the system parameters, in order to estimate their uncertainties and correlations. We choose models yielding reasonably small χ_ν^2 as the best-fitting solutions.

What separates the planetary migration (step I) from the orbital optimization (step II) is the scale-free property of the N-body Newtonian dynamics. In the barycenter frame, they read as

$$\ddot{\boldsymbol{r}}_i = k^2 \sum_j m_j \frac{\boldsymbol{r}_{ji}}{|\boldsymbol{r}_{ji}|^3}, \quad i \neq j = 0, \ldots, N, \qquad (2)$$

where $\boldsymbol{r}_{ji} \equiv \boldsymbol{r}_j - \boldsymbol{r}_i$ is the relative radius vector from a body i to a body j, where $i, j = 0$ denotes the star; m_j are for the masses ($m_0 \equiv m_\star$); and k^2 is the gravitational constant. The scaling invariance of the particular ordinary differential equations (ODEs), here Equation (2), means that if a particular $\boldsymbol{r}_i(t)$ is the solution to these equations, then $\rho_{\rm a}^{-2/3} \boldsymbol{r}_i(\rho_{\rm a} t)$ with some fixed and constant scaling factor $\rho_{\rm a} > 0$ is also the solution.
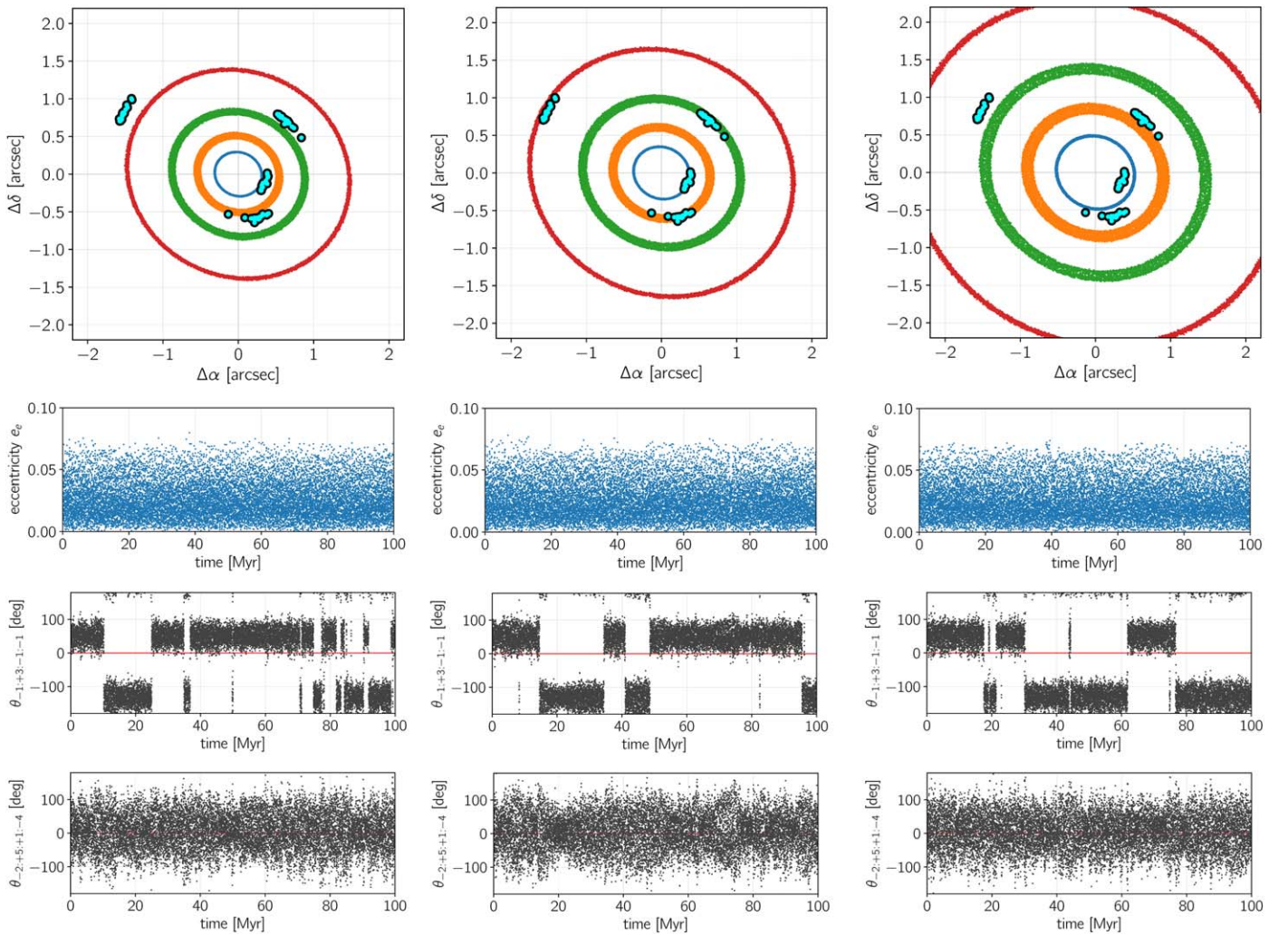
Figure 4. Illustration of scale-free dynamics at the second step of MCOA. Initial semimajor axes in a resonant configuration of four planets, shown in the middle column, are linearly scaled by factors of 0.8 (left column) and 1.33 (right column). We selected two critical arguments of the generalized Laplace resonance, $\theta = \lambda_1 - 3\lambda_2 + \lambda_3 + \lambda_4$ and $\theta = 2\lambda_1 - 5\lambda_2 - \lambda_3 + 4\lambda_4$ (two middle rows), which librate with similar amplitudes (two bottom rows). The innermost eccentricity (second row from top), shown as an example, varies within similar limits.

Therefore, the orbital radii, or orbital arcs at prescribed time intervals, may be scaled by the same factor but with an appropriate time change. Such a geometrically rescaled copy of the orbits exhibits the same dynamical character as the original system.

The N-body ODE scaling invariance is illustrated in Figure 4. By following a migrating planetary configuration, we usually end up with too-compact (left column) or too-wide (right column) orbits with respect to the observations. In fact, these configurations are rescaled copies, by a factor of 0.8 and 1.33, respectively, of the directly simulated system in the middle column. Apparently, it fits relatively well to the observations. This resonant configuration has been obtained through a fast migration during only 1.8 Myr. In spite of a substantial scaling, the dynamical character of all configurations is preserved for at least 100 Myr: the critical angles of the zeroth-order generalized Laplace resonance (Papaloizou 2015) oscillate around the same center, and the eccentricities vary within the same limits (middle and bottom rows in Figure 4).

We note that the reference configuration is weakly chaotic in the sense of a small mLCE. However, in this Lagrange-stable configuration, all orbits remain bounded for a very long time.

The system remains stable since it is resonant, actually in an unusual way—one of the critical arguments librates around the same libration center, while the second one "switches" between two centers. This example is selected intentionally to show that even weakly chaotic configurations may be scaled without losing any of the geometric features, like the critical angles or eccentricity evolution.

The scale-free dynamics property releases us from an uncertainty of the star distance. The present determination of the parallax $\pi = 24.22 \pm 0.09$ mas ($\sim$41.3 pc) in the GAIA Data Release 2 catalog (Gaia Collaboration et al. 2018) places the system almost 2 pc farther than assumed in the literature to date, $d = 39.4$ pc (van Leeuwen & Fantino 2005). The relatively significant correction of the parallax has essentially no implication for the orbital models; besides, the planetary masses may be larger due to a correction for the absolute luminosity.

3. The Best-fitting Orbital Model

We searched for the best-fitting solutions to the astrometric measurements in Konopacky et al. (2016) with the approach described above. Homogeneous observations of the HR 8799

system in Konopacky et al. (2016) were obtained between 2007 and 2014 with NIRC2 on the Keck II telescope and the same reduction pipeline. The data are corrected for systematic biases present in the observations in the discovery papers (Marois et al. 2008, 2010). The Keplerian (kinematic) solutions in Konopacky et al. (2016) favor coplanar, low-eccentric orbits, as well as agree to within 1σ with the 8e:4d:2c:1b resonance model; hence, our assumptions are supported by their independent analysis.

We aim to verify whether the MCOA model of these observations, which are a subset of the data available to date and gathered in Wertz et al. (2017; their Appendix), may be extrapolated and fit all measurements made by different authors with other instruments. We also found a significant deviation of the synthetic model orbit IVa in Goździewski & Migaszewski (2014) for the outermost planet, which systematically precedes the latest observations in Maire et al. (2015) and Pueyo et al. (2015). The new analysis could improve the previous model.

Among the found solutions, we selected the best-fitting configuration yielding $\chi_\nu^2 \simeq 0.87$. Its osculating elements at epoch $t_0 = 2004.532$ of the first observation in Konopacky et al. (2016), as determined from the primary fit parameter $\boldsymbol{p}$, are displayed in Table 1 (model IV$_K$). We found tens of geometrically similar configurations within $\chi_\nu^2 \simeq 1$; therefore, we focus on this particular basis configuration. This model, representing the 8e:4d:2c:1b MMR chain, is similar to the best-fitting solution IVa in Goździewski & Migaszewski (2014). Yet we note a smaller value of the initial semimajor axis $a_4 \simeq 67$ au. We examined this difference closely. As expected, the new solution improves the astrometric model by providing a better match to the first and last observations at epochs of 1998.83 and 2014.93 in the whole data set, respectively. Indeed, it removes the systematic trend and the "too-fast" orbital motion of planet b predicted by our earlier model IVa.

3.1. Measuring the Stability of Orbital Solutions

In order to reveal the global dynamical structure of the system, we use the fast indicator technique, besides the direct integration of the equations of motion. The idea behind this approach relies on determining the character of motion (chaotic or regular) on relatively short orbital arcs. A configuration classified as fast indicator–stable for a relatively short motion time of $\simeq 10^4$ outer periods may be extrapolated for a 10–100 longer Lagrange stability time (also called the event time, T_E), implying noncrossing, noncolliding, and bounded orbits. Usually, the fast indicators are related either to the mLCE (Cincotta & Simó 2000; Goździewski et al. 2008) or to a diffusion of the fundamental frequencies (Laskar 1993).

As the fast indicator, essentially equivalent to the mLCE, we use the mean exponential growth factor of nearby orbits (MEGNO, hereafter $\langle Y \rangle$) developed by Cincotta & Simó (2000) and Cincotta et al. (2003). It is implemented in our message passing interface parallelized code μFarm. The required system of the equations of motion and their variation equations may be integrated with the BSG scheme (Hairer et al. 2002). We also used the symplectic algorithm (Goździewski et al. 2008), which is much more CPU-efficient, but it might be nonreliable in strongly chaotic zones where collisional events are possible. We decided to use the BSG scheme for the final experiments to avoid such numerical and artificial biases.

For brevity, orbital configurations are called $\langle Y \rangle$-stable if $|\langle Y \rangle - 2| < \epsilon$, where $\epsilon \simeq 0.05$, for a particular number of characteristic periods, counted in 10^4 outermost planet orbits. The MEGNO integrations were stopped if $|\langle Y \rangle - 2| > 5$, and we consider such configurations unstable ($\langle Y \rangle$-unstable). As we found in previous papers, $\langle Y \rangle$-stable models are equivalent to Lagrange-stable solutions for intervals of time 1–2 orders of magnitude longer.

More details on these MEGNO calibrations to determine the Lagrange stability regarding the HR 8799 system, as well as low-mass planet systems, were discussed in our earlier papers (Goździewski et al. 2008; Goździewski & Migaszewski 2014), as well as in a new work (Panichi et al. 2017). We also note that MEGNO has been recently used as a reference tool by Hadden & Lithwick (2018), who developed a new quasi-analytic stability criterion for eccentric two-planet systems.

3.2. The MCMC Experiment Setup

We conducted follow-up MCMC experiments aiming to determine the orbital parameter uncertainties for stable solutions found with MCOA and demonstrate the degree of instability of the four-planet system. For that purpose, we performed single-temperature MCMC sampling with the `emcee` package (Foreman-Mackey et al. 2013). Recalling our results in Goździewski & Migaszewski (2014), the orbital elements in stable four-planet models may only be varied within tiny ranges. Here we release the coplanarity constraint and search for stable solutions around the best-fitting model IV$_K$. The Bayesian inference makes it possible to introduce prior information, like indirect observational constraints. For instance, the debris disk geometry determined independently of the imaging astrometry is reported to be almost coplanar with the planetary orbits and seen at a position angle around $50°$–$60°$ (Matthews et al. 2014; Booth et al. 2016). Therefore, the debris disk models could impose additional, indirect constraints on the inclination I and nodal angle Ω of the system.

With the MCMC sampling of the parameter space, stable planetary configurations might be detected, perhaps relatively distant from the model IV$_K$ in Table 1. Therefore, in the search for stable solutions, we conducted the MCMC sampling with up to 2048 `emcee` walkers initiated in a small hyper-cube in the orbital parameter space centered at the best-fitting model for 128,000–256,000 iterations each, mostly limited by CPU-demanding stability checks made with the MEGNO indicator. We evaluated χ_ν^2 and the likelihood function $\log \mathcal{L} \sim -\chi_\nu^2/2$ required to compute the posterior distribution. In this experiment, the masses of the planets and all orbital elements are considered as free parameters of the astrometric model.

In order to narrow the parameter space and reduce possible degeneracies, we imposed Gaussian priors $\mathcal{N}(\mu, \sigma_\mu)$ with the mean μ equal to the best-fitting values in Table 1. As for the variances σ_μ, we chose the following: for the masses, $\sigma_m = 3\, m_{\text{Jup}}$; for the semimajor axes, $\sigma_a = 5$ au; for the Poincaré elements, $x_i = e_i \cos \omega_i$ and $y_i = e_i \sin \omega_i$, $\mu_{x,y} = 0$ and $\sigma_{x,y} = 0.3$; and for the inclinations and nodal longitudes, $\sigma_I = 30°$ and $\sigma_\Omega = 60°$. The priors have been set as improper (uniform) for the osculating mean anomalies at the initial epoch, $\mathcal{M}_i \in [0°, 360°)$, $i = 1, \ldots, 4$.

During the MCMC sampling with the Gaussian priors, we also evaluated the MEGNO of all solutions with $\chi_\nu^2 < 2.6$ to determine the limits of the stability zone around the best-fitting stable solution. The $\langle Y \rangle$ integration time was set to $\simeq 7000$ outermost periods, hence permitting marginally Lagrange-stable models. In accordance with our earlier experiments (Goździewski & Migaszewski 2014), the $\langle Y \rangle$ integration

Table 1
Osculating Elements of the Best-fitting Four- and Five-planet Solutions

	m ($m_{\rm Jup}$)	a (au)	e	I (deg)	Ω (deg)	ϖ (deg)	$\mathcal{M}$ (deg)
	Model IVa at Epoch of 1998.83, $m_\star = 1.56\,M_\odot$ (Figure 7, top row, and Figure 12)						
HR 8799e	9 ± 2	15.4 ± 0.2	0.13 ± 0.03			176 ± 6	326 ± 5
HR 8799d	9 ± 3	25.4 ± 0.3	0.12 ± 0.02	25 ± 3	64 ± 3	91 ± 3	58 ± 3
HR 8799c	9 ± 3	39.4 ± 0.3	0.05 ± 0.02			151 ± 6	148 ± 6
HR 8799b	7 ± 2	69.1 ± 0.2	0.020 ± 0.003			95 ± 10	321 ± 10
	Model IV$_{\rm K}$ at Epoch of 2004.532, $m_\star = 1.52\,M_\odot$, $\chi^2_\nu = 0.87$, $\nu = 97$, dim$\boldsymbol{p} = 5$ (Figures 8–11)						
HR 8799e	9.4 ± 0.5	15.45 ± 0.25	0.127 ± 0.011			107.5 ± 1.5	13.7 ± 1.5
	9.426	15.45001	0.12696			107.54637	13.67259
HR 8799d	8.2 ± 0.8	25.36 ± 0.30	0.095 ± 0.006			26.9 ± 2.5	79.4 ± 3.0
	8.185	25.35505	0.09540			26.94575	79.41486
HR 8799c	6.9 ± 0.5	39.78 ± 0.40	0.048 ± 0.005	25 ± 2	64 ± 5	105.8 ± 2.0	137.2 ± 5.0
	6.857	39.77699	0.04829	25.289	64.414	105.79908	137.18943
HR 8799b	6.7 ± 0.5	67.01 ± 0.35	0.023 ± 0.003			120.1 ± 3.0	235.7 ± 5.0
	6.680	67.00881	0.02297			120.07543	235.66545
HR 8799fA	1.660	115.25600	0.02222			174.59807	54.13554
HR 8799fB	0.660	116.43105	0.02222			174.59807	54.13554
HR 8799fC	1.000	134.16610	0.02218	25.289	64.414	11.33805	327.42380
HR 8799fD	0.330	133.86900	0.02218			11.33805	327.42380
HR 8799fE	0.100	137.76200	0.02218			11.33805	327.42380
	Model IV$_{\rm MCMC}$ at Epoch of 2004.532, $m_\star = 1.52\,M_\odot$, $\chi^2_\nu = 0.98$, $\nu = 74$, dim$\boldsymbol{p} = 28$ (Figure 6)						
HR 8799e	9.5 ± 0.5	15.48 ± 0.25	0.123 ± 0.011	26 ± 2	64 ± 5	110.2 ± 1.5	12.5 ± 1.5
	9.489	15.48223	0.12278	26.138	63.612	110.23990	12.49904
HR 8799d	7.5 ± 0.8	25.35 ± 0.30	0.097 ± 0.006	29 ± 2	56 ± 5	33.1 ± 2.5	80.8 ± 3.0
	7.490	25.35133	0.09669	29.096	56.160	33.05848	80.78110
HR 8799c	7.1 ± 0.5	39.95 ± 0.40	0.046 ± 0.005	25 ± 2	63 ± 5	104.8 ± 2.0	140.0 ± 5.0
	7.082	39.94936	0.04629	25.318	62.732	104.77760	139.98150
HR 8799b	6.8 ± 0.5	67.11 ± 0.35	0.024 ± 0.003	31 ± 2	60 ± 5	118.5 ± 3.0	242.9 ± 4.5
	6.753	67.11155	0.02358	30.517	59.595	118.49210	242.91630
	Model V$_{\rm A}$ at Epoch of 1998.83, $m_\star = 1.52\,M_\odot$, $\chi^2_\nu = 2.71$, $\nu = 229$, dim$\boldsymbol{p} = 5$ (Figure 7, middle and bottom rows)						
HR 8799e	9.450	15.45863	0.09789			115.18157	330.89613
HR 8799d	6.851	25.59693	0.09300			29.67592	62.45914
HR 8799c	7.121	39.78074	0.05227	26.103	60.210	101.42421	136.56084
HR 8799b	8.847	70.24633	0.05055			52.58777	306.83016
HR 8799f	2.500	111.48326	0.01205			140.41787	65.69502

Notes. For Model IVa, reproduced from Goździewski & Migaszewski (2014), the osculating epoch is 1998.83, and the stellar mass $m_\star = 1.56\,M_\odot$. Model IV$_{\rm K}$, found in this work, is determined at the osculating epoch of 2004.532 and for the star mass of $m_\star = 1.52\,M_\odot$. Coplanar solutions postscripted with "A," "B," "C," "D," and "E" extend Model IV$_{\rm K}$ with a fifth hypothetical planet in a stable orbit. Model IV$_{\rm MCMC}$ is a non-coplanar four-planet stable solution with small $\chi^2_\nu \simeq 1$ found with the MCMC sampling around Model IV$_{\rm K}$. These models are solutions to the measurements in Konopacky et al. (2016). Model V$_{\rm A}$ is a preliminary fit to all observations collected in Wertz et al. (2017) and found with the MCOA for a five-planet system. Uncertainties for parameters in Models IV$_{\rm K}$ and IV$_{\rm MCMC}$ are determined as ranges of $\langle Y \rangle$-stable samples yielding $\chi^2_\nu < 1.6$ around their median values. Formal errors, determined as the 16th and 86th percentiles of the samples, are 2–3 times smaller. For reference, parameter values for fits IV$_{\rm K}$, IV$_{\rm MCMC}$, and V$_{\rm A}$ with five digits after the decimal point are provided, as literally used in our experiments. Parameter $\nu = N_{(\alpha, \delta)} - {\rm dim}\boldsymbol{p}$ is for the degrees of freedom, where $N_{(\alpha, \delta)}$ denotes the number of (α, δ) measurements, and dim$\boldsymbol{p}$ is the number of free parameters.

interval should be safely longer than 10^4 characteristic periods, in order to determine long-term Lagrange-stable configurations for at least 160 Myr. The $\langle Y \rangle$-stable solutions for 7000 outermost orbits should provide a Lagrange stability time that is 10 times longer (at least $\simeq 30$ Myr).

For reference, we also performed the MCMC sampling with all priors uniform and determined wide parameter ranges spanning 24 $m_{\rm Jup}$ for masses m_i and 30 au for semimajor axes a_i around their best-fitting values IV$_{\rm K}$ in Table 1, as well as x_i, $y_i \in [0,\ 0.67]$ for the Poincaré elements, $I_i \in [0°,\ 90°]$, $\Omega_i \in [0°,\ 180°]$, and $\mathcal{M}_i \in [0°,\ 360°]$ ($i = 1, \ldots, 4$).

We tried to estimate the autocorrelation time $\tau_{\rm emcee}$ through sampling experiments without stability checks, in order to reduce the CPU overhead. We increased the chain length up to 512,000. We used the method of Sokal (1996), as proposed by Foreman-Mackey et al. (2013) in the recent version of the emcee sampler. We found that $\tau_{\rm emcee}$ is typically very long and varies between $\sim 40{,}000$ and $\sim 120{,}000$ for different elements and priors. The second parameter expressing the sampling "health," the acceptance rate, was typically well below 0.2, unless the emcee scaling parameter $a_{\rm emcee}$ was set to low values of ~ 1.2. Similarly difficult and ill-conditioned
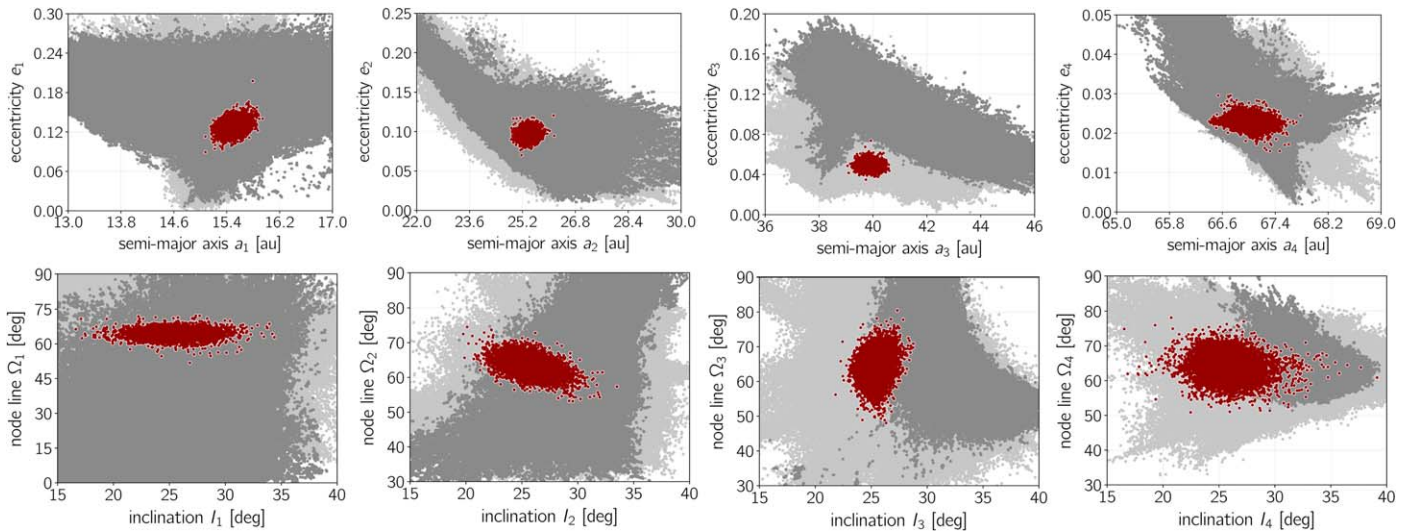
Figure 5. Results of MCMC experiments as 2-dim χ_ν^2 projections of samples onto selected parameter planes. Light and dark gray filled circles mark solutions derived with uniform priors with $\chi_\nu^2 < 1.6$ and $\chi_\nu^2 < 0.74$, respectively. Red filled circles are for $\langle Y \rangle$-stable models with $\chi_\nu^2 < 2.6$. See Figure 6 for the sky-plane representation of configurations selected from the illustrated samples.

Monte Carlo and MCMC sampling experiments are reported by Konopacky et al. (2016) and Wertz et al. (2017) regarding kinematic (Keplerian) models.

We found a particularly strange discrepancy of the distribution of the node arguments Ω_i. As reported in Konopacky et al. (2016), two Ω_i peaks wide for up to a few tens of degrees are centered around roughly $\sim 60°$ and $\sim 130°–150°$ for all planets but HR 8799d, with one much wider dominant peak around $\Omega_d \sim 100°$. The first mode around $\sim 60°$ is consistent with the outer debris disk orientation (Matthews et al. 2014; Booth et al. 2016). However, it is missing among all single-mode posteriors of Ω_c and Ω_e derived by Wertz et al. (2017). We note here that our N-body MCMC experiments made with fixed masses in the best-fitting solution IV_K that could mimic the Keplerian model but with Gaussian priors on the eccentricity reveal a two-modal posterior only in Ω_c, while all remaining peaks of $\Omega_{b,d,e}$ are found between $50°$ and $60°$. This strongest two-modal distribution of Ω_c divided by a shallow posterior valley might explain a low acceptance rate in our experiments. Also, a dynamical sense of the second mode of $\Omega_i \simeq 130°$, implying mutually inclined orbits, remains uncertain.

3.3. The MCMC Experiments and the Best-fitting Model

Our results derived in two example MCMC experiments are illustrated in Figure 5 as 2-dim χ_ν^2 distributions for selected parameters. The light gray filled circles represent solutions with $\chi_\nu^2 < 1.6$, and dark gray filled circles are for samples with $\chi_\nu^2 < 0.74$, derived with uniform priors. We note that the lowest $\chi_\nu^2 \simeq 0.60$. The red filled circles mark solutions with $\chi < 2.6$ that are $\langle Y \rangle$-stable for ~ 7000 outer periods when Gaussian priors are set only for masses and semimajor axes. The number of illustrated samples is $\sim 2 \times 10^6$.

Clearly, even for the very limited $\chi_\nu^2 < 0.74$ range, the model parameters are practically unbounded. They vary in wide limits both for the uniform and for the Gaussian priors. Also, the 1-dim posterior distributions (not shown) imply that the N-body astrometric model is unconstrained, similar to the Keplerian models in Konopacky et al. (2016) and Wertz et al. (2017). Stable solutions are found only relatively close to the initial resonant

configuration, and the overall shape of the stable, compact zones agrees with the results derived with a constrained genetic algorithm (see Goździewski & Migaszewski 2014 for details). Here, however, the search for stable non-coplanar solutions has been performed with an independent method.

We performed the same experiment for different choices of the Gaussian priors (the mean values and their σ_μ) for masses and orbital elements. All these attempts to find stable configurations resulted in outputs qualitatively similar to those demonstrated in Figure 5. We estimate that the total number of tested samples with $\chi_\nu^2 < 2.6$ has reached 10^9 in more than 20 MCMC experiments performed on 256 CPU cores each. We did not find any $\langle Y \rangle$-stable models beyond a close neighborhood of the best-fitting, stable resonant model IV_K. Therefore, finding a stable configuration by chance or without imposing tight or a priori constraints on the model parameters would be extremely difficult.

Finally, the results of the MCMC sampling experiments shown in Figure 5 are further illustrated in Figure 6. We selected 20 stable solutions with $\chi_\nu^2 < 1.04$ and 500 other (unstable) models with low $\chi_\nu^2 < 0.74$ from the MCMC-derived posterior samples. Their orbital arcs, marked with red and gray curves, respectively, are overplotted on the astrometric data in Konopacky et al. (2016) as blue circles and all other measurements in the literature collected in Wertz et al. (2017) as yellow diamonds. In spite of the tight restriction, $\chi_\nu^2 < 0.74$, the gray curves span a wide region of the sky. Moreover, stable models to a subset of data in Konopacky et al. (2016) extrapolate very well to the full data set. We may note the proper timing of the synthetic orbits both with the most recent and with the earliest measurements (top middle, top right, and bottom left panels in Figure 6).

An interesting conclusion is given in the top middle panel for planet HR 8799d. Low $\chi_\nu^2 < 0.74$ solutions (dark curves) are widely spread around the *Hubble Space Telescope* (*HST*) observation at epoch 1998.98 in Lafrenière et al. (2009). However, stable, resonant models pass in the middle of these solution orbits, close to the *HST* measurement made a few years before. It might be a lucky coincidence, but we recall that stable solutions are extrapolated back from the model epoch of
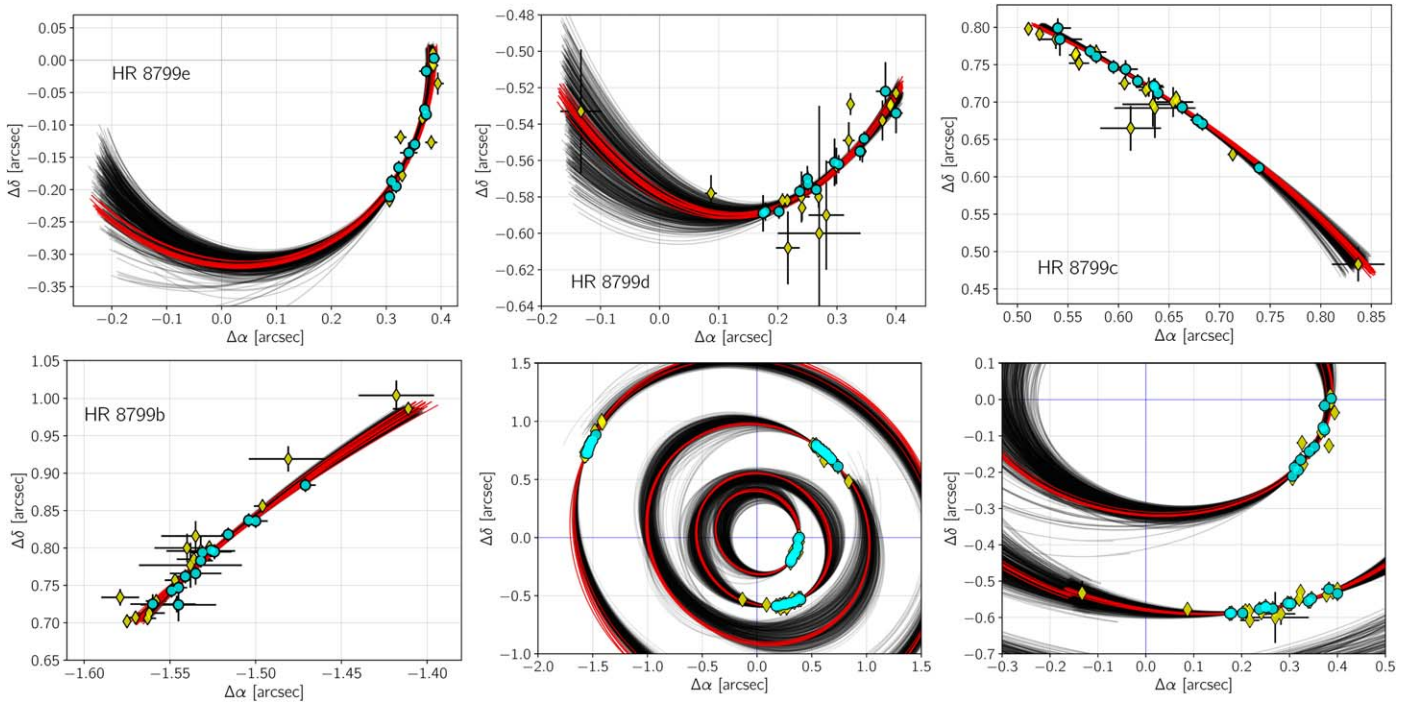
Figure 6. Best-fitting solution to the four-planet model illustrated at the sky plane. The *y*-axis corresponds to N, and the *x*-axis corresponds to E (note that the numerical values of $\Delta\alpha$ are sign-opposite regarding the formal left-hand direction of the right ascension α). Blue circles are for measurements in Konopacky et al. (2016), and yellow diamonds are for measurements in other papers, as collected in Wertz et al. (2017). Red curves mark several stable solutions with $\chi^2_\nu \simeq 1$ from the MCMC sampling. Gray curves are for orbital arcs derived from unstable models within $\chi^2_\nu < 0.74$, marginally worse from $\chi^2_\nu \simeq 0.6$ for the mathematically best-fitting *N*-body solutions. All model orbits have been derived for measurements in Konopacky et al. (2016) and then extended between the epochs of 1998.83 and 2014.93 in the full data set in Wertz et al. (2017). The osculating epoch is 2004.532, i.e., the first epoch in Konopacky et al. (2016).

2004.532, and the *HST* measurement was not included in the optimization.

One more feature of stable solutions is illustrated in the bottom right panel of Figure 6, showing model orbits for the two inner planets. In this panel, each of the orbits is computed for its osculating period. Surprisingly, orbital arcs of stable solutions for planet HR 8799d do not close. It means that the gravitational interactions may be detected even within the narrow observational window. It is also a warning that kinematic models that do not account for the mutual planetary interactions may soon be inadequate on a longer time basis.

In order to summarize, we consider the results of our MCMC experiments mostly as an attempt at determining the range of stable islands, rather than a rigorous optimization and statistical inference presented in Pueyo et al. (2015), Konopacky et al. (2016), and Wertz et al. (2017). Moreover, since stability zones are extremely tiny with respect to wide posteriors, the results of statistically reliable MCMC sampling made with the kinematic orbital model (without stability checks) might bring only limited information on stable solutions.

4. The $\langle Y \rangle$-model of Debris Disks

Having the long-term stable configurations of the system, we may simulate debris disks in a framework of the restricted and nonrestricted problems. In the first version, massless particles (asteroids) are influenced by the gravitational tug of the planets (primaries), and we assume that the asteroids do not attract the planets or mutually interact. In the second, nonrestricted case, hypothetical massive bodies may be added to the system of observed planets. Such bodies may be detected indirectly through resolving the global architecture of the observed

system. For instance, a signature of the fifth planet beyond HR 8799b may be the radius of the inner edge of the outer debris disk (Booth et al. 2016). Also, Wilner et al. (2018) constrained a mass of the outer planet HR 8799b to $\simeq 6\,m_{\rm Jup}$ through modeling the inner edge with ALMA and VLA observations. Based on the ALMA observations alone, Read et al. (2018) deduced a mass of an additional planet, HR 8799f, beyond the orbit of planet b.

We conducted extensive Monte Carlo simulations of the debris disks in both frameworks. The initial semimajor axis, eccentricity, and orbital phases are drawn randomly within prescribed ranges. These elements extend the initial condition for the observed planets (primaries), and the resulting orbits are integrated. We then analyze a large volume of the initial conditions with two numerical methods.

For simulating the debris disk as the restricted problem, we use the direct *N*-body integrations with the hybrid scheme in the `Mercury 6.3` package (Chambers 1999), corrected by de Souza Torres & Anderson (2008). This approach is common in the literature (e.g., Contro et al. 2016; Read et al. 2018). We fixed the step size of 64 days for the mixed-variables leapfrog (MVS) and the local accuracy $\epsilon = 10^{-13}$ in the BSG algorithm, providing a relative energy error as small as 10^{-9}.

The second numerical model makes use of the fast indicator idea and relies on determining the stability of the test orbits through their $\langle Y \rangle$-signatures, following arguments in Section 3.1. We call the approach the $\langle Y \rangle$-model hereafter.

The results of simulations, which are osculating orbital elements of stable systems, are projected onto the Cartesian coordinate (x, y) plane and shown in the semimajor axis–eccentricity (a, e) plane. It helps to reveal and identify resonant structures in the phase space.

We conducted two CPU-intensive tests on up to 256 CPU cores to validate the $\langle Y \rangle$-model for the debris disk through the direct numerical integrations. Computations are carried out for the fixed masses of the bodies moving in the same plane.

4.1. The Restricted Four-planet System

In the first test, including four planets, we conducted a number of Mercury 6.3 runs with up to 4096 massless particles each. Our primary goal of this and further experiments is to reconstruct the inner edge of the outer disk; hence, we limit the semimajor axes to a smaller range than predicted for the whole radius as large as ~450 au. Beyond the inner region of the disk, filled with strong MMRs, the population of asteroids might be determined with some quasi-analytic distribution (Booth et al. 2016; Read et al. 2018).

In order to compare the results with findings in earlier papers, the initial conditions of the planets in this experiment are the same as in the best-fitting model IVa in Goździewski & Migaszewski (2014); see also Table 1. We integrated the orbits of primaries and massless particles for 34 Myr, which may be considered the low limit of the system age. The simulation has been restricted to the inner part of the disk, i.e., the initial semimajor axes $a_0(t=0) \in [60, 150]$ au. We sampled eccentricities $e_0(t=0) \in [0, 0.33]$, as well as orbital phases randomly, with $\varpi_0, \mathcal{M}_0 \in [0°, 360°]$.

The total number of particles traced with the direct N-body integration was $\simeq 6 \times 10^5$. Figure 7 shows two snapshots of the simulation, at $t = 7$ Myr (top left panel) and at the end of the integration interval, $t = 34$ Myr (top right panel). They represent instant coordinates of massless asteroids that have not been ejected beyond 1000 au. The final snapshot encompasses 3.7×10^5 objects surviving the integration.

The MEGNO test is illustrated in the top middle panel of Figure 7. Almost 10^6 particles with $\langle Y \rangle$ are marked at the integration time of 7 Myr, which corresponds to ~14,000 orbital periods of the outermost planet and roughly 8000 revolutions at $\simeq 100$ au. Particles marked as $\langle Y \rangle$-stable for that interval should persist for a more than 10 times longer interval in Lagrange-stable orbits, roughly 60–70 Myr. Indeed, the inner border of the debris disk derived with the direct Mercury 6.3 integration looks very similar to the non-circular oval shape revealed by the $\langle Y \rangle$-model.

A different density of particles in the two snapshots may be explained by a sampling strategy. In regions where the test orbits are strongly chaotic, like just beyond the orbit of HR 8799b, the motion is $\langle Y \rangle$-unstable during short intervals $\simeq 0.1$ Myr, and the $\langle Y \rangle$ integration may be stopped as soon as $\langle Y \rangle > 5$, safely larger than $\langle Y \rangle \simeq 2$ for stable systems. That made it possible to examine huge sets of $\sim 10^8$ initial conditions, orders of magnitude larger than could be sampled with the direct N-body integrations. Such strongly chaotic regions are explored in a CPU-efficient way, and we argue that the inner complex edge may be revealed in more detail with the $\langle Y \rangle$-model.

We also note similarly extended Lagrange islands L_4 and L_5 of stable particles, indicating a sensitivity of the $\langle Y \rangle$ indicator for unstable solutions.

The $\langle Y \rangle$-model plot at the (x, y) plane of Cartesian coordinates may be understood as a snapshot of all possible stable (quasi-periodic, regular) orbits of the probe masses with various orbital phases and eccentricity for the same values of the semimajor axis. These orbits might be populated in a real system, but not necessarily. The actual population of asteroids may depend on the prior planetary system history, its migration, and the locally variable density of asteroids.

4.2. The Restricted Five-planet System

We also made a second $\langle Y \rangle$-calibration test with essentially the same settings but for a preliminary five-planet model of the observations in Wertz et al. (2017) found with the MCOA. The parameters of this solution are displayed in Table 1 as model V$_A$. In this model, a hypothetical, yet-undetected 2.5 $m_{\rm Jup}$ planet at $a_{\rm f} \simeq 111.5$ au forms the 16e:8d:4c:2b:1f MMR chain with the observed planets. The test particles were integrated with the Mercury 6.3 code for an interval of 68 Myr, even longer than before, but for the same interval of 7 Myr with the μFarm MEGNO code.

The results are shown in the bottom row of Figure 7. We sampled asteroid orbits with $a_0(t=0) \in [60, 220]$ au and $e_0 \in [0, 0.4]$, implying the initial orbits up to the collision zone with the orbit of planet f. Also in this case, although the $\langle Y \rangle$-interval is relatively short, the results of the direct N-body integrations and from the Monte Carlo $\langle Y \rangle$-sampling closely overlap. Even subtle structures, such as a narrow arc made of particles opposite the position of HR 8799b, are clearly present in the last two panels. Also, the overall egg-like shape of the inner edge looks the same. Initially massive L_4 and L_5 Lagrangian clumps of asteroids in the bottom left panel are finally reduced to smaller, dispersed islands with similarly wide centers, as seen in the bottom right panel. These islands appear as much more compact structures in the $\langle Y \rangle$-model plot (bottom middle panel). This implies that particles initially forming a kind of echo around L_4 and L_5 corotation centers in the direct integration plot (bottom left panel) are secularly unstable. They are eventually removed from the system.

We projected the Keplerian elements of the test particles at the (a_0, e_0) plane, as shown in the bottom row of Figure 7. The distribution of the elements derived with short-term $\langle Y \rangle$-integrations (bottom middle panel) closely matches with the data after 68 Myr found directly with the Mercury 6.3 code. We note a two-modal structure of the 1:1 MMR (bottom middle $\langle Y \rangle$ panel), which has been detected with a dense sampling of the particles. The distribution of elements appears diffuse due to their representation in the common astrocentric Keplerian frame (Lee & Peale 2003). It hinders the true resonant structure of the disk, and we address this issue further in Sections 6 and 7.

One should be aware that the $\langle Y \rangle$-model is in regard to the short-term resonant dynamics (e.g., Laskar & Robutel 2001), and the relatively short integration times may not be sufficient to resolve long-term secular resonances present in all systems with more than two planets (e.g., Morbidelli 2002). However, since the obtained $\langle Y \rangle$-distribution of elements overlaps with the results of the direct N-body integrations, the dynamical effects of the secular resonances are either nondetectable during ~70 Myr or overlap with the short-term MMR dynamics.

5. The Inner Disk Dynamical Structure

In order to even better validate the $\langle Y \rangle$-model, we compared its outcomes with the results in a recent work by Contro et al. (2016), regarding the inner debris disk in the HR 8799 system (Reidemeister et al. 2009; Su et al. 2009; Hinkley et al. 2011; Matthews et al. 2014). Its structure is not yet fully resolved.
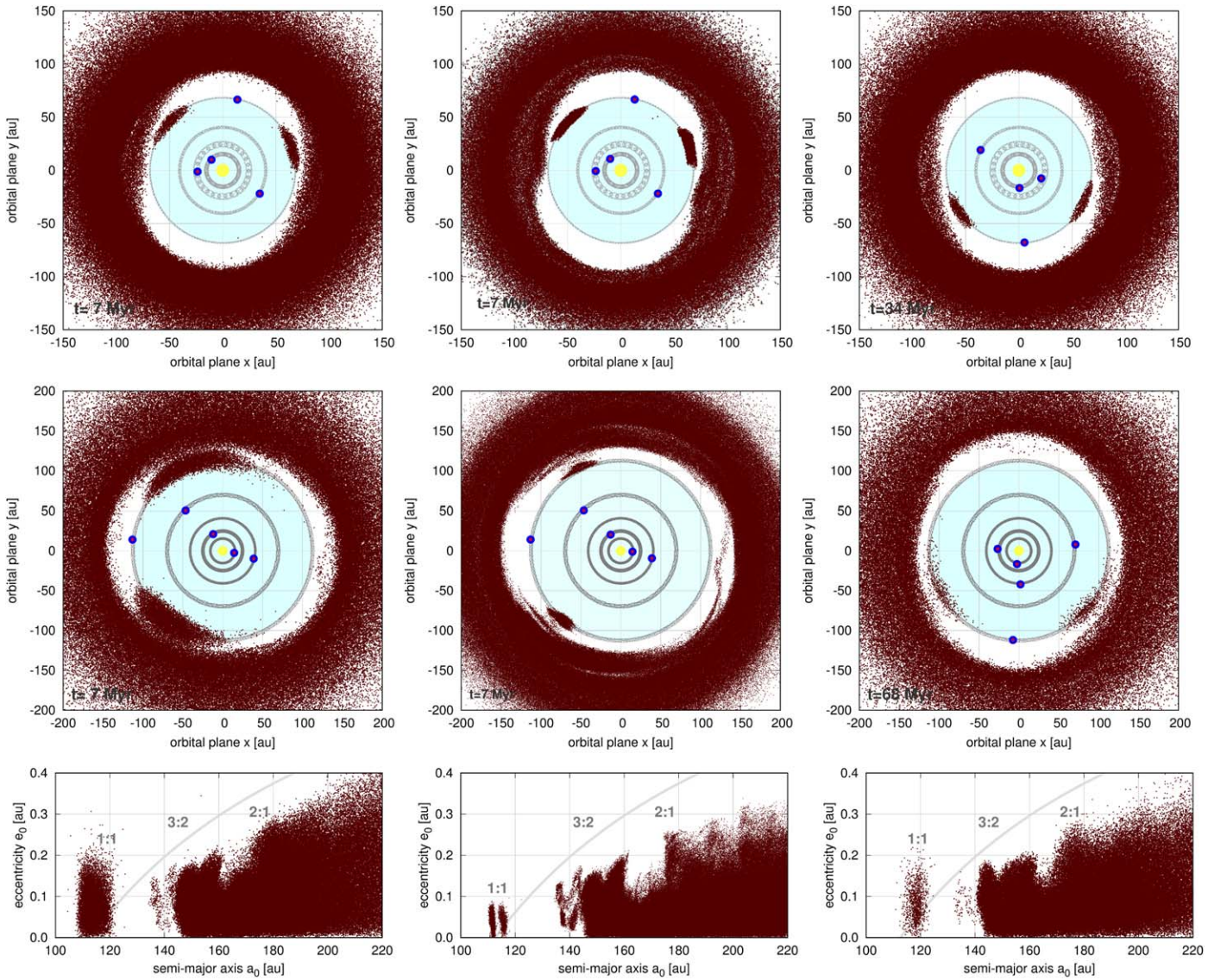
Figure 7. Top row: outer debris disk of the four-planet HR 8799 system, in accord with model IVa in Goździewski & Migaszewski (2014). The left-hand and right-hand panels show snapshots of the astrocentric coordinates (x, y) of massless asteroids at the orbital plane at times $\simeq 7$ and $\simeq 34$ Myr, respectively, derived with the direct N-body integrations conducted with the Mercury 6.3 package (the hybrid scheme). Filled circles are for the positions of the planets, and light gray curves are orbital arcs sampled for the time span $\simeq 34$ Myr. The final snapshot involves 370,000 massless particles that survived the integration. The middle panel shows the astrocentric coordinates (x, y) of $\simeq 10^6$ test particles with masses 10^{-15} m_{Jup} in $\langle Y \rangle$-stable orbits. Middle row: outer debris disk of the five-planet HR 8799 model V_A (Table 1). The left-hand and right-hand panels show snapshots of the astrocentric coordinates (x, y) of massless asteroids at the orbital plane at motion times $\simeq 7$ and $\simeq 68$ Myr, respectively. Planet orbits are sampled and marked with gray dots for $\simeq 68$ Myr. The final snapshot involves 125,000 massless particles that survived the integration. The middle panel is for astrocentric coordinates (x, y) of $\simeq 1.5 \times 10^6$ test particles with masses 10^{-15} m_{Jup} in $\langle Y \rangle$-stable orbits. Integrations were done with the μFarm package. Bottom row: osculating, astrocentric Keplerian elements of the massless particles in the (a_0, e_0) plane in the five-planet model (middle row). The light gray curve marks the collision curve with planet HR 8799e. Approximate positions of low-order MMRs with this planet are labeled.

We conducted experiments for a varied mass of test particles: small, essentially massless asteroids of $m_0 = 10^{-15}$ m_{Jup}, a super-Earth with $m_f = 10$ M_{Earth}, and an $m_f = 1$ m_{Jup} Jovian planet. We investigated a zone beyond 4 au from the star up to 2 au beyond the inner orbit of HR 8799e ($\simeq 17$ au) and orbits with $e_{0.f} \in [0, 0.4]$ roughly within the collision zone with the orbit of planet e. As before, we aim to resolve the outer edge of the disk, which is carved by the closest planet and the whole system indirectly, through the coupled resonant motion. The initial conditions for the primaries are the same as in our new astrometric model IV_K (Table 1).

The results are illustrated in Figure 8. In all panels, the innermost planet HR 8799e is marked with a filled circle.

The left-hand column of panels is for the restricted problem. The orbits of planets HR 8799e,d are sampled and marked with gray dots for the integration interval of 3 Myr. That corresponds to 40,000 revolutions of the innermost perturber HR 8799e and more than 4000 revolutions of the outermost planet b. The (x, y) plots, representing stable orbits at the initial osculating epoch, are accompanied by the final distribution of the astrocentric Keplerian elements in the (a_0, e_0) plane for massless objects and the (a_f, e_f) plane for non-zero-mass planets (the two remaining columns).

Although the mass of the fifth body is varied, the inner disk reveals similar features determined by low-order MMRs with the innermost planet e. By including massless particles with moderate eccentricities $e_0 \in [0, 0.4]$ in the initial distribution,
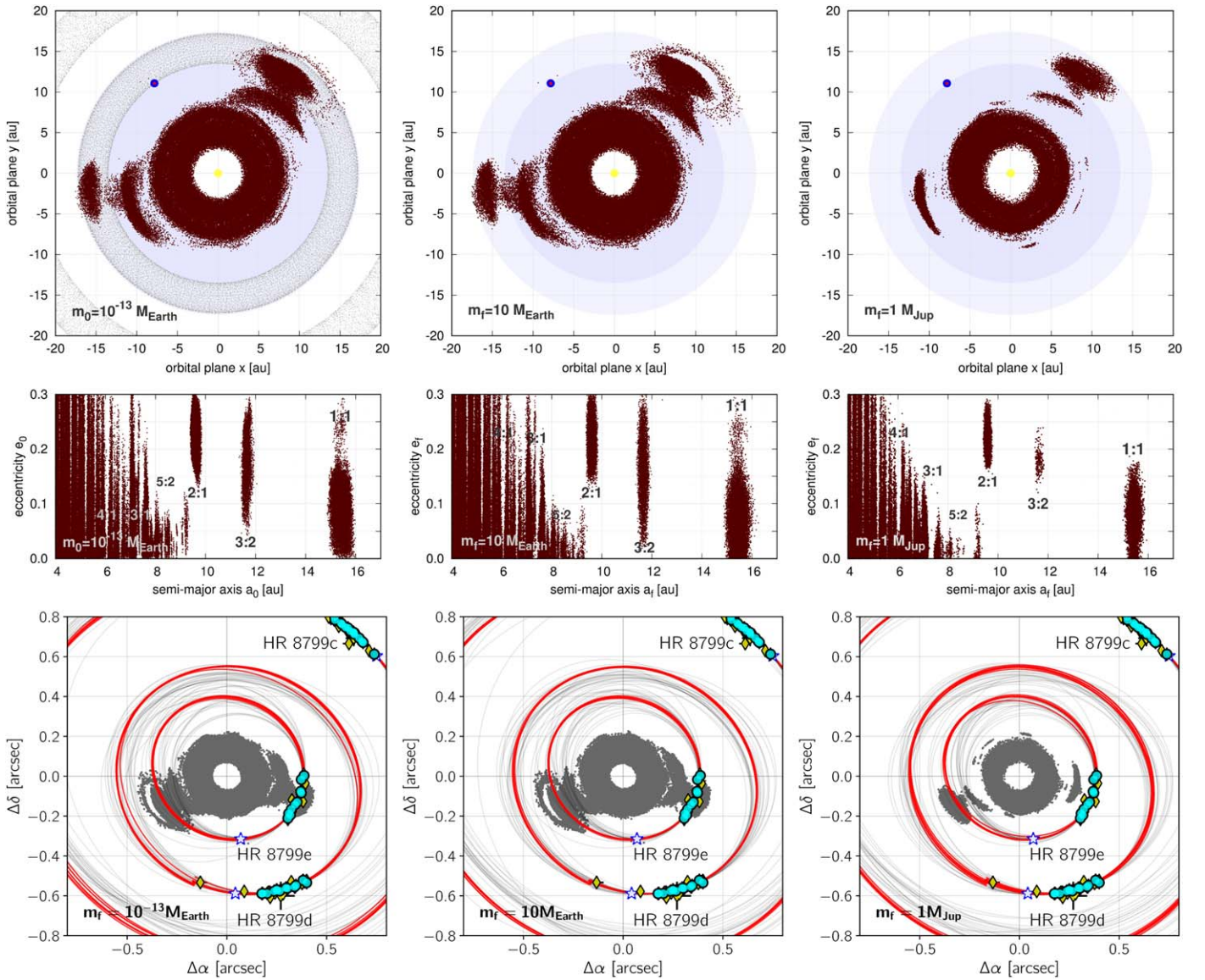
Figure 8. Inner debris disk (left column) and possible orbits of the yet-undetected innermost planet HR 8799f (middle and right columns) in model IV_K at the initial osculating epoch 2004.532. Panels in the top row are for instant astrocentric (x, y) coordinates for different masses of test bodies in stable orbits. The left column is for $10^{-15} m_{Jup}$, the middle column is for $10 M_{Earth}$, and the right column is for $1 m_{Jup}$. A filled circle marks the initial position of the planet HR 8799e. Light gray dots in the top left panel illustrate the orbits of two inner planets sampled for the integration time of 3 Myr. For reference, light blue disks in the next two panels mark the nominal periastron and apastron distance of HR 8799e. Panels in the middle row are for the (a_0, e_0) or (a_f, e_f) planes of the initial Keplerian elements with labels identifying low-order MMRs with the innermost planet HR 8799e. Panels in the bottom row are for the (x, y) coordinates rotated to the sky plane, in which the y-axis corresponds to N and the x-axis corresponds to E (note that the numerical values of $\Delta\alpha$ are sign-opposite with respect to the formal left-hand direction of the right ascension α). Astrometric observations in Konopacky et al. (2016) are marked with filled circles, and other measurements listed in Wertz et al. (2017) are marked with diamonds. Several models selected from the MCMC sampling are marked with red (stable, $\chi_\nu^2 \simeq 1$) and gray (unstable, $\chi_\nu^2 < 0.74$) curves. For reference, the positions of planets HR 8799c,d,e at the initial epoch of 2004.532 are marked with star symbols. Note the variability of unstable models, in spite of relatively small χ_ν^2. Snapshots in subsequent panels illustrate $\sim$250,000, $\sim$240,000, and $\sim$220,000 $\langle Y \rangle$-stable orbits, respectively, for 3 Myr ($\simeq$6 × 10^4 and $\simeq$3 × 10^4 revolutions of the two closest perturbers, HR 8799e,d).

we obtain a highly asymmetric shape of the outer parts of the disk, with large Lagrangian L_4, L_5 clumps accompanied by complex structures of the 3:2 MMR with the innermost planet e. We note that the overall border of the disk edge is different from that found by Contro et al. (2016), who also mapped the phase space with the $\langle Y \rangle$-indicator. By fixing the initial phases of the asteroids in 2-dim scans, one obtains nonexhaustive representation of stable regions. For instance, the 3:2 MMR is missing at the (a_0, e_0) scans shown in Contro et al. (2016).

The $\langle Y \rangle$-model is also useful to "predict" the positions of a hypothetical innermost, yet-undetected fifth planet "f" in the system. Such a body has been considered an explanation of the observed spectral energy distribution (SED) in Su et al. (2009) and Hinkley et al. (2011). In Goździewski & Migaszewski (2014), we simulated such a body with the MCOA algorithm, and we found a few possible locations of the missing planet associated with low-order 2:1 and 3:1 MMRs with HR 8799e.

However, the gravitational influence of such a hypothetical planet on the inner companion HR 8799e could hardly be
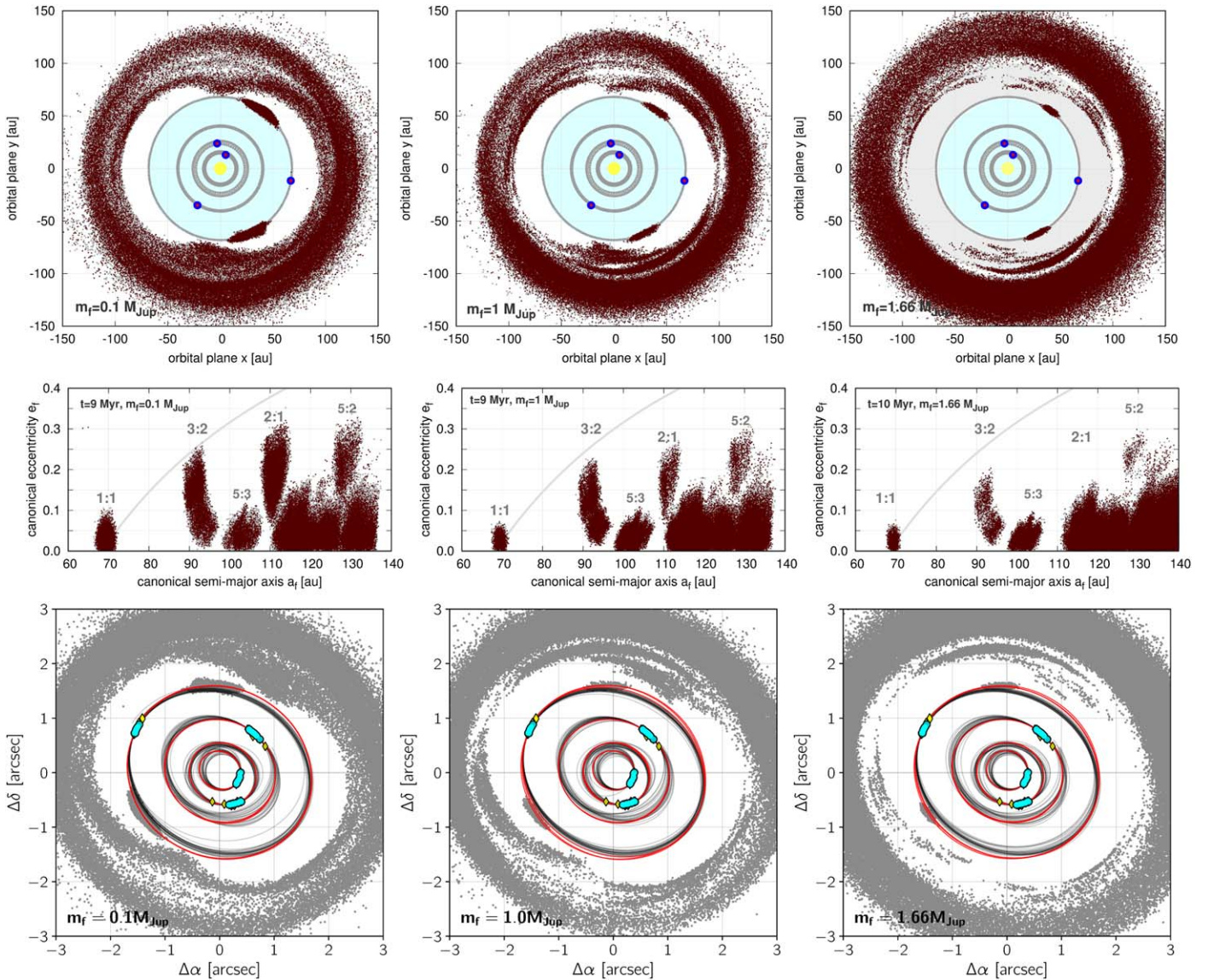
Figure 9. The ⟨Y⟩-model simulations of localizations of a putative planet HR 8799f in the outer region of the system. Subsequent panels show astrocentric coordinates (x, y) of stable orbits in the orbital plane (top row), a distribution of the Poincaré canonical orbital elements (a_f, e_f) (middle row), and a projection of the instant coordinates at the sky plane relative to the observed system (filled circles) and several four-planet synthetic orbits from the MCMC sampling, marked with red and gray curves for stable and unstable models, respectively. The y-axis corresponds to N, and the x-axis corresponds to E (note that the numerical values of $\Delta\alpha$ are sign-opposite with respect the formal left-hand direction of the right ascension α). Columns are for different masses of the putative planet of 0.1, 1, and 1.66 m_{Jup}. Light gray curves in the middle row indicate the collision curve for planet HR 8799e and test objects. Integrations are done with the μFarm package with the MEGNO indicator for 9 and 10 Myr. Gray rings in the top panels illustrate the sampled orbits of the observed planets for the integration time. The snapshots show up to 2×10^5 objects in ⟨Y⟩-stable orbits. The reference epoch 2004.532 is the date of the first observation in Konopacky et al. (2016).

detected through deviations of astrometric measurements, given short orbital arcs and relatively large uncertainties. We can simulate potential locations of the hypothetical planet more efficiently with the ⟨Y⟩-model, attributing nonzero mass to the "asteroids." We conducted such experiments for $m_f = 10$ Earth masses and $m_f = 1$ m_{Jup} (middle and right columns of Figure 8, respectively). The most noticeable phase-space structures are preserved and look similar to the restricted case. The additional putative planet should be involved in two-body MMRs with the inner observed planet HR 8799e at orbits down to $a_f \simeq 6$ au. It also means that the four-planet model is robust against perturbations. These predictions overlap with our earlier simulations in Goździewski & Migaszewski (2014).

We note that attempts to detect or dismiss the hypothetical inner fifth planet have failed so far. This planet is below detection limits due to small mass or too-close proximity to the star and insufficient contrast (Skemer et al. 2012; Matthews et al. 2014; Maire et al. 2015; Zurlo et al. 2016).

The bottom panels in Figure 8 are for the sky-projected snapshots of stable orbits at the initial epoch of 2004.532 (marked with stars), overplotted with several model orbits from the MCMC sampling and all measurements in Wertz et al. (2017). These plots might be useful in interpreting the direct-imaging observations. Down to $\simeq 7$–8 au ($\simeq 0\farcs2$), the "missing" planet may be found in discrete, isolated islands associated with 3:2, 2:1, 5:2, and 3:1 MMRs with planet e. Below that

limit, it could persist essentially everywhere in a wide ring around the star.

6. The Outermost Planet V Hypothesis

The inner edge of the outer cold debris disk has been detected at 145 au, hence much farther than the $\simeq 90$ au that could be explained by the gravitational pull of planet HR 8799b (Booth et al. 2016; Read et al. 2018). With the same framework and orbital model IV_K of the primaries as in the previous section regarding the inner disk structure, we aim to investigate locations of a hypothetical fifth planet, HR 8799f, exterior to HR 8799b. We computed the $\langle Y \rangle$-model for a few choices of the mass m_f of the putative planet. The results are illustrated in Figure 9 for $m_f = 0.1$, 1, and 1.66 m_{Jup}, respectively, and we made a similar experiment for $m_f = 2.5\, m_{Jup}$ (not shown).

The top row in Figure 9 illustrates possible stable positions of HR 8799f in the orbital plane at the initial epoch of 2004.532. Again, it should be understood as a representation of the initial conditions implying stable evolution of the system, rather than a physical disk. The distribution of orbits is very similar to that derived for massless or low-mass asteroids shown in Figure 7. In order to understand the dynamical structure of this quasi-disk, we also plotted the same orbits projected onto the (a_f, e_f) plane (middle row), where a_f and e_f are the canonical Poincaré elements (Morbidelli 2002; Goździewski et al. 2008). This parameterization of the orbital elements is critical to "disen-tangle" the structure of MMRs. Otherwise, a classification of orbits is obscure with the common Keplerian astrocentric elements due to significant variation of the osculating semimajor axes of the outer planets (for instance, Lee & Peale 2003); see also the bottom row in Figure 7.

As can be deduced from Figure 9, a Neptune-mass planet could belong to a stable system when involved in a low-order two-body resonance with HR 8799b, like the 1:1, 3:2, 5:3, 2:1, and 5:2 MMRs. In that instance, the eccentricity of the fifth planet could be as large as $e_f \simeq 0.3$. It might be found at essentially any location at the sky (see the bottom row) beyond the angular distance roughly equivalent to the semimajor axis of $a_f \simeq 90$ au. Also, two Trojan 1:1 MMR locations are possible. A similar, extended, yet more sparse and clear pattern of the MMRs is present for a larger mass of 1 m_{Jup} (middle column), as well as for 1.66 m_{Jup} (right column) and 2.5 m_{Jup} (not shown).

7. The Outer Debris Disk Structure

Finally, we conducted $\langle Y \rangle$-model simulations for a few copies of the HR 8799 best-fitting solution, model IV_K in Table 1, involving the fifth planet with different masses and the initial semimajor axis. As shown in the previous section, such a planet is weakly constrained by the present astrometry. However, recent observations of the outer disk imply conjugated constraints for its structure, as well as for the possible orbit and mass of this putative object.

We aim to simulate the outer disk composed of probe masses m_0 set to $10^{-15}\, m_{Jup}$ in further experiments. After selecting a mass and orbital elements of the fifth, additional planet HR 8799f from simulations described in Section 6 and illustrated in Figure 9, we verified $\langle Y \rangle$ scans in the (a_f, e_f) plane. We checked whether its stability zone is sufficiently wide to avoid biases due to a proximity to unstable resonances. When necessary, the semimajor axis a_f has been slightly modified to separate it safely from all nearby unstable MMRs. The orbital elements of the

primaries selected for computations are gathered and labeled in Table 1 as HR 8799fA to HR 8799fE, complementing model IV_K. We tested orbits with the initial $a_{0,k} \in [60, 240]$ au and eccentricities $e_{0,k} = [0, \sim 0.5]$ below the collision curve with the outer planet. (For the massless particles, we distinguish the Poincaré canonical elements (a_p, e_p) from $(a_0, e_0) \equiv (a_k, e_k)$ denoting common Keplerian astrocentric elements.)

The first set of simulations is illustrated in Figure 10. Here we essentially repeated the $\langle Y \rangle$-calibrating experiment in Section 4 but to determine the edge of the outer disk with the updated model IV_K. The (x, y) snapshot of stable orbits at the initial osculating epoch of 2004.532 is now complemented by the (a_p, e_p) plane for the canonical Poincaré elements of the orbits of test particles at the end of the integration interval of 10 Myr, extended to more than 10^4 orbits at ~ 100 au. The integration time implies that orbits characterized as $\langle Y \rangle$-stable should be Lagrange-stable for $\simeq 100$ Myr. The (x, y) orbits are coded in a color-scale representing their initial Keplerian astrocentric eccentricity e_k. This provides additional informa-tion on the distribution and geometry of stable orbits at the initial epoch of 2004.532.

The (x, y) orbital plane shown in the top left panel in Figure 10 reveals similar features to those seen in Figure 7 (top row). The shape of the inner edge of the disk, resembling a fat peanut, is strongly distorted by the orbits of asteroids in the 3:2 and 5:3 MMRs with HR 8799b. They may be easily identified in the (a_p, e_p) plot. There are also large islands of stable particles corotating with the L_4, L_5 Lagrangian points of planet b. They extend for wide arcs as long as $\simeq 40$ au. The short-term dynamics in the 100 Myr timescale is apparently governed by the major gravitational pull of HR 8799b, since stable orbits are possible essentially only below the collision curve $e_p(a_p)$, marked in the bottom row in gray. This curve is determined from $a_b (1 + e_b) \simeq a_p (1 - e_p)$. Some proportion of the asteroids might move on moderately eccentric orbits up to $e_p \simeq 0.4$ when trapped in low-order MMRs.

The two next columns in Figure 10 are for five-planet systems with planet HR 8799fA of mass $m_f = 1.66\, m_{Jup}$ and planet HR 8799fB of mass $m_f = 0.66\, m_{Jup}$, respectively (see model IV_K in Table 1). The semimajor axis $a_f \sim 116$ au, forming the 16e:8d:4c:2b:1f MMR chain, is almost the same in both experiments. These configurations address the inner edge at $\simeq 145$ au, as detected in Booth et al. (2016). Indeed, for $m_f = 1.66\, m_{Jup}$, stable orbits exhibit semimajor axes $a_p > 140$ au, beyond the Lagrangian L_4, L_5 zones, with two strongly resonant regions of the 3:2 and 2:1 MMRs with planet HR 8799f. A similarity of the (x, y) distribution with the results in the middle panels of Figure 7 is striking. The inner edge would be strongly distorted by moderately eccentric orbits $e_p \simeq 0.2$ associated with the 3:2 MMR. A ring of eccentric 2:1 MMR orbits with $a_p \simeq 150$ au is marked with reddish points in the top middle panel. The Lagrangian zones are much wider than in the four-planet configuration (panels in the left column of Figure 10) and extend along arcs of ~ 100 au, contributing to an even more noncircular and asymmetric inner edge of the disk.

An even more complex inner shape appears for smaller mass $m_f = 0.66\, m_{Jup}$ of the hypothetical planet HR 8799f at $a_f \simeq 116$ au (right column). While the inner edge in the (a_p, e_p) plane is similar to the $m = 1.66\, m_{Jup}$ case, now the 4:3 MMR is populated with more particles. Also, the Lagrange zones are more extended, and moderately eccentric orbits in the 4:3 MMR form two clumps
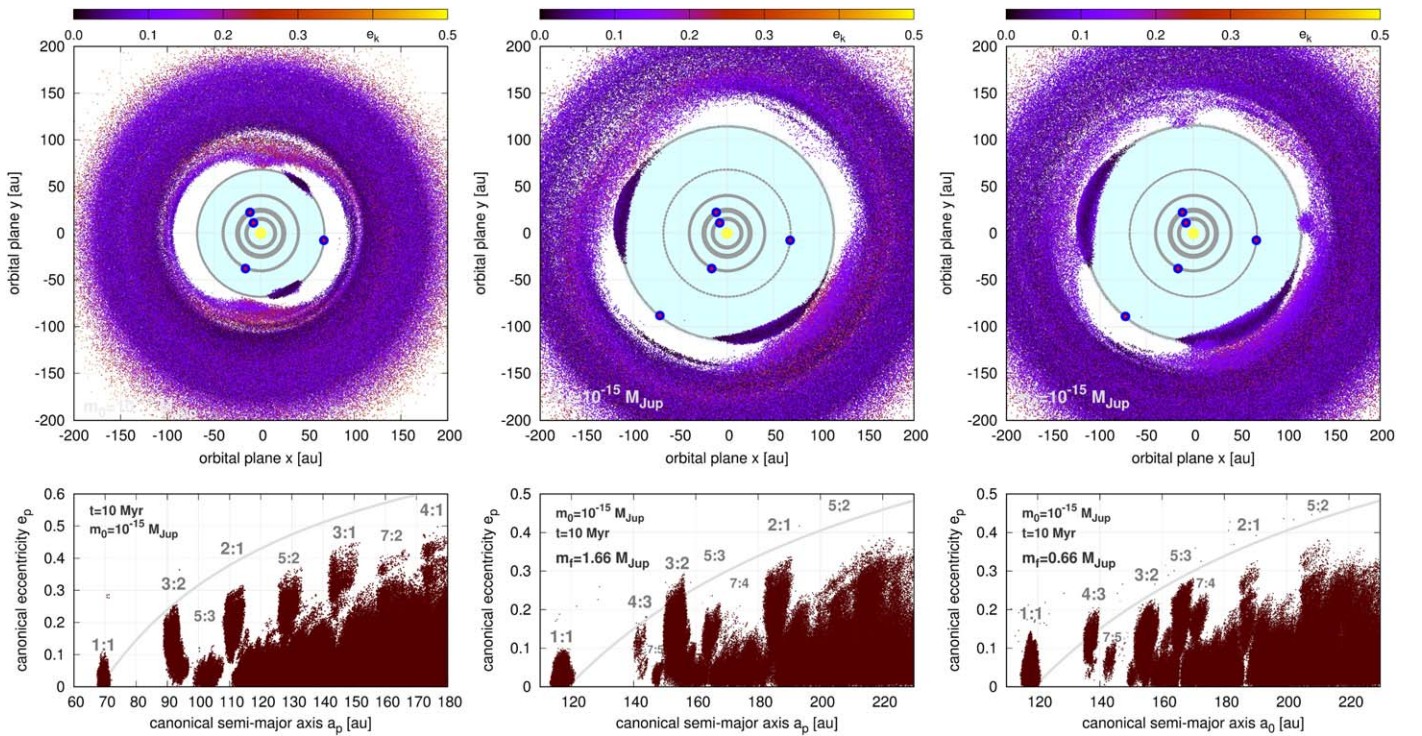
Figure 10. Inner part of the outer debris disk of the four-planet (left column) and five-planet systems (middle and right columns). Orbital elements of the fifth planet, complementing model IV_K, are listed as HR 8799fA and HR 8799fB in Table 1. Subsequent panels in the top row show astrocentric coordinates (x, y) of asteroids in $\langle Y \rangle$-stable orbits for different masses of a hypothetical companion HR 8799f at the initial epoch of 2004.532. Panels in the bottom row are for the canonical Poincaré elements (a_p, e_p) of these stable solutions at the end of the integration interval of 10 Myr. Gray lines are for the collision curve of orbits with planet HR 8799f. The low-order MMRs with planet HR 8799f are labeled in the bottom panels. Osculating initial orbital eccentricities e_k at the initial epoch are color-coded in the top row. Snapshots in subsequent panels illustrate $\sim 920{,}000$, $\sim 580{,}000$, and $\sim 910{,}000$ $\langle Y \rangle$-stable orbits.

opposite the planet at distances equal to its mean heliocentric semimajor axis a_f. Other features of the asteroid distribution are similar to the previous case.

We also considered an orbital setup with the outer planet f beyond $\simeq 130$ au, as predicted by the disk models in Booth et al. (2016) and Read et al. (2018). Due to the larger semimajor axis of the perturber, the $\langle Y \rangle$-integration time has been increased to 12 Myr ($\sim 10^4$ orbits of the outermost perturber at ~ 130 au). We investigated three cases with $m_f = 1$, 0.33, and 0.1 m_{Jup}, illustrated in the columns of Figure 11. While the overall shape of the disk is roughly similar to that of the previous models, new features appear. The inner edge becomes more and more distorted from a circle for decreasing masses m_f. Simultaneously, clumps of stable orbits associated with the Lagrangian equilibria develop into a state in which they are merged with the inner edge at the mean distance equal to the semimajor axis a_f. Also, the low-order MMR zones are even better isolated; hence, the inner edge up to $\simeq 220$ au is strictly resonant.

The most complex image of the inner border of the disk has been found for the smallest mass of $m_f = 0.1\, m_{Jup}$, placed at $a_f \simeq 138$ au. This particular configuration follows the best-fitting solution explaining the recent ALMA observations in Read et al. (2018). The resonant structure associated with this planet is also very sharp, yet some particles may survive in stable, resonant orbits between planets HR 8799b and HR 8799f. We did not find such orbits for $m_f = 0.33\, m_{Jup}$ (not shown), although planet f is shifted by only $\simeq 5$ au. The inner resonant orbits are associated with 1:1, 3:2, and 5:2 MMRs with planet HR 8799b. In both

zones, the eccentricities might be excited beyond collision curves with planets HR 8799b and HR 8799f.

8. The Debris Disk under Migration

The resonant nature of the four-known-planet configuration might result from the migration due to the planet–disk interactions. Including this process in the debris disk formation scenario may potentially shift the border with respect to the results of the previously studied models, in which all the planets are statically placed at their current orbits together with a disk of the massless particles. We therefore aim to investigate whether migration of the planets might place the inner edge of the outer debris belt at ~ 145 au. Then the requirement for an additional planet outside the orbit of planet b could be released. While the analysis is preliminary, it might offer an alternative scenario for explaining the ALMA observations.

We assume that the planets are initially located outside their current positions, and they undergo the inward convergent migration that is supposed to form a chain of 2:1 MMRs. We use the same model of the planet–disk interactions as used before and described by Equation (1) but with κ the same for all planets.

Although the massless particles are too small to undergo the type I migration, they could, in principle, "feel" the gas drag (Adachi et al. 1976). The timescales of the orbit decay that results from the drag depend strongly on the particle masses, as well as on the gas densities (the volume densities, not the surface densities, as for the type I and type II migration). Assuming that the surface gas density $\propto r^{-3/2}$ and the total gas mass within the (10, 100) au range equals $1\, m_{Jup}$ when we start

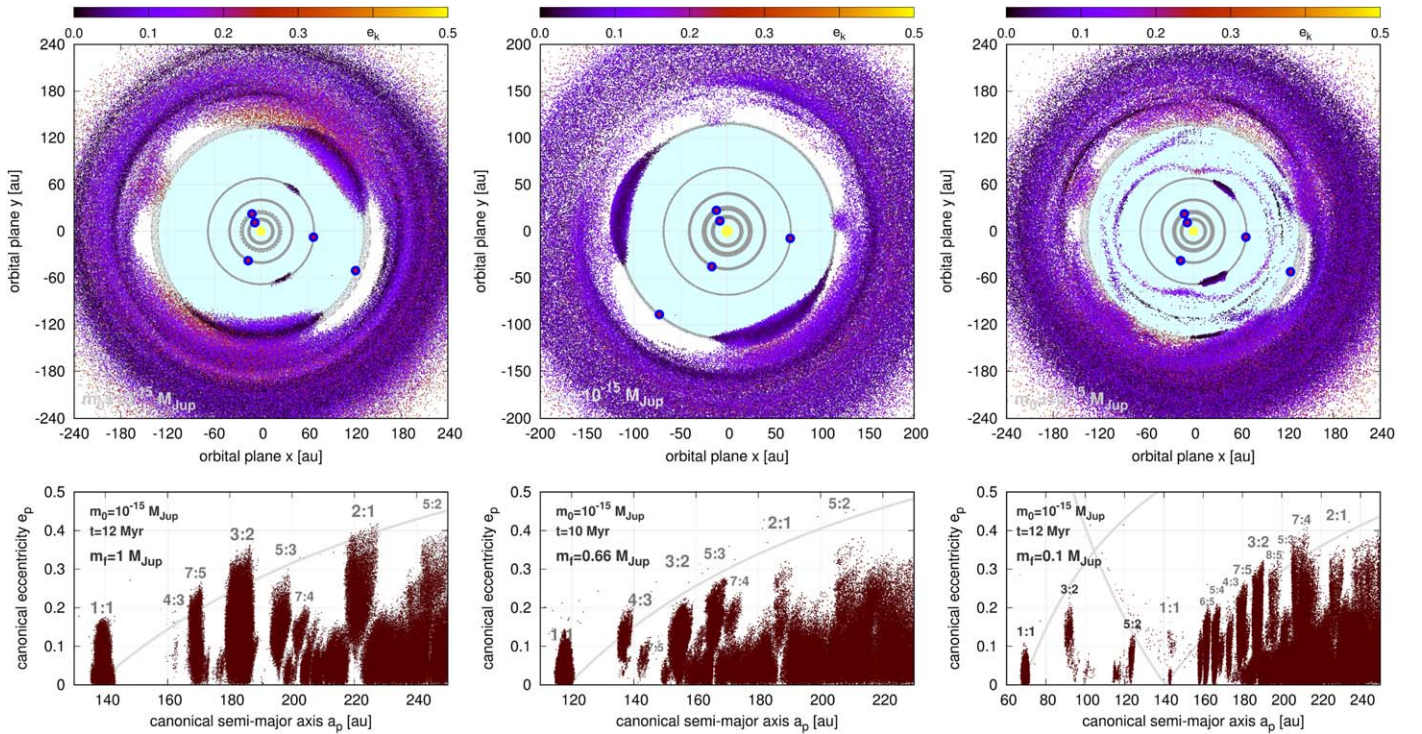**Figure 11.** Inner part of the outer debris disk of the five-planet systems and different masses $m_f = 1$, 0.33, and 0.1 m_{Jup} of a hypothetical fifth planet beyond the orbit of HR 8799b. Orbital elements of the fifth planet, complementing model IV$_K$, are listed as HR 8799fC, HR 8799fD, and HR 8799fE in Table 1. A mass of this additional planet is labeled in the bottom panels. Subsequent panels in the top row show astrocentric Cartesian coordinates (x, y) of asteroids at $\langle Y \rangle$-stable orbits for different masses m_f of a hypothetical companion HR 8799f, labeled in subsequent bottom panels, at the initial epoch of 2004.532. Panels in the bottom row are for the canonical Poincaré elements of these stable solutions at the end of the integration intervals of 10 and 12 Myr. Gray lines are for collision curves of orbits with planets HR 8799f and HR 8799b (right column). Low-order MMRs with planets HR 8799f and HR 8799b are labeled. Osculating astrocentric eccentricities e_k at the initial epoch are color-coded in the top row. Snapshots in subsequent panels illustrate $\sim$980,000, $\sim$635,000 and $\sim$500,000 $\langle Y \rangle$-stable orbits, respectively.

the simulation, the volume gas density would be in the range of 10^{-14} to 10^{-15} g cm^{-3}, depending on the assumed aspect ratio between 0.01 and 0.1. For particles larger than a meter, the characteristic timescale of the orbit decay induced by the gas drag would be greater than the age of the system and the migration timescales assumed for the planets that are $\sim$10 Myr. Therefore, we neglect the migration of the massless particles in this model.

We performed a series of simulations for different initial orbits and the migration parameters. We assume that the resulting system has to be resonant and of a similar size as the observed configuration, and the inner edge of the massless particle disk has to place in the range of (145 ± 12) au, as determined by Booth et al. (2016). These constraints do not permit for very wide initial orbits, since the resulting inner edge would be placed outside the observed border. On the other hand, all the pairs of planets need to be located outside 2:1 MMRs, as the resonances are formed in the process of the convergent migration. Moreover, the innermost planet should start the migration beyond its current position at $\sim$15.5 au.

All the constraints given above limit the initial orbits significantly. After a series of experiments, we found an initial configuration and the migration parameters that fulfill the criteria. The evolution of the four-planet system into the resonant configuration is shown in the left-hand column of Figure 12. The initial semimajor axes and other parameters are given in the caption of the figure. The outermost planet starts the migration at 90 au and the innermost one at 17.5 au. The migration timescales between 9 and 28 Myr (from the outermost to innermost planets), together with the disk decay

timescale of 1 Myr, make the planets migrate inward by a distance of $\sim$20 au for the outermost and $\sim$2 au for the innermost planets. The resonance (with a low-amplitude libration of the resonant angle) is formed after $\sim$1 Myr of evolution; therefore, the final system of four planets is long-term stable.

The process of the resonant chain formation needs a comment. Entering into the resonant chain of four planets is a chaotic process; therefore, even small changes in the initial configuration, as well as differences between the numerical integrators used to solve the equations of motion, may lead to different results. For instance, the resonance may not be achieved, resulting in further self-disruption of the system. This is why the evolution shown here has to be treated as an example configuration. Initial configurations different from the one presented, as well as different migration parameters, may lead to qualitatively similar results.

Apart from the planets, there are a number of massless objects included in the model whose motion is being perturbed by the planets. Their final distribution after 10 Myr of the integration is shown in the middle and right columns of Figure 12. We chose a uniform distribution of the particle semimajor axes ranging from 15 to 429 au (the latter is the outer edge of the debris belt found by Booth et al. 2016). Initial eccentricities of the particles range from 0 to 0.03 (middle column) and from 0 to 0.3 (right column); all the angles are chosen randomly in the whole range of $(0°, 360°)$. The final number of objects that remained in the system was $\sim$10^5 in each case. The inner edge of the asteroid belt places itself at $\sim$145 au for both ranges of the initial eccentricities. The border
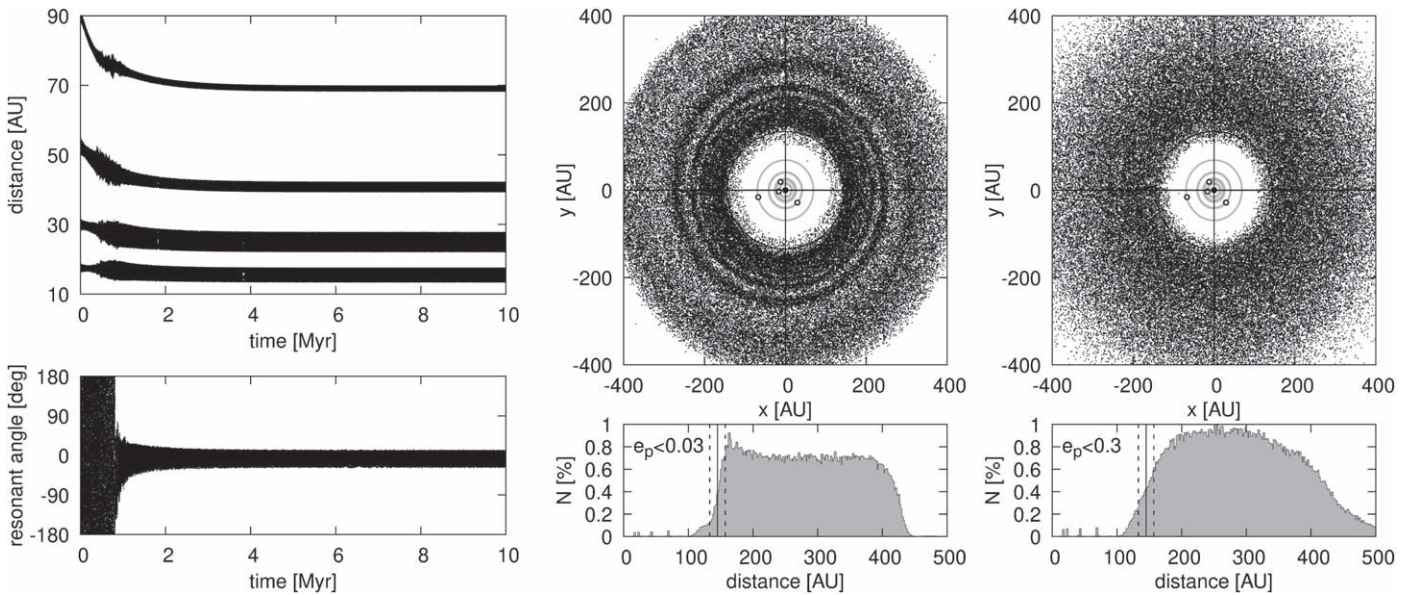
Figure 12. Left column: evolution of an example initial configuration that ends up as a system resembling the configuration of HR 8799. Initial semimajor axes are $a_1 = 17.5$, $a_2 = 30$, $a_3 = 52$, and $a_4 = 90$ au. All eccentricities and arguments of pericenters are initially 0. Mean anomalies are chosen to be 0°, 90°, 180°, and 170° from the innermost to the outermost planets. The migration parameters are $T = 1$ Myr, $\kappa = 200$, and respective timescales of migration $\tau_1 = 28$, $\tau_2 = 18$, $\tau_3 = 12$, and $\tau_4 = 9$ Myr. The masses are the same as in solution IVa in Goździewski & Migaszewski (2014; see also Table 1), i.e., $m_\star = 1.56\,M_\odot$, $m_1 = m_2 = m_3 = 9\,m_{\rm Jup}$, and $m_4 = 7\,m_{\rm Jup}$. The top panel presents the evolution of the astrocentric distances of the planets, while the bottom panel illustrates the evolution of the resonant angle of the double Laplace resonance, i.e., $\theta = \lambda_1 - 2\lambda_2 - \lambda_3 + 2\lambda_4$. Middle and right columns: final distribution of asteroids after 10 Myr of evolution. The top panels present the positions of the asteroids in the orbital plane (dots), together with the positions of the planets (open circles). Gray rings show the temporal positions of the planets integrated over 100 Myr after the migration stops. The black circle indicates the inner border of the outer debris disk of HR 8799 found in Booth et al. (2016), i.e., 145 au. The bottom panels present histograms of the asteroids' astrocentric distances. Vertical lines indicate the debris disk border (solid line) and the uncertainties (dashed lines), i.e., (145 ± 12) au. The initial asteroids' eccentricities were chosen from the ranges of [0, 0.03] (middle column) and [0, 0.3] (right column).

is sharper for the simulations with initial $e < 0.03$. Moreover, in this case, there are spiral waves in the disk, while when initial $e < 0.3$, the disk is axially symmetric.

In both cases, there is a small number of objects inside 145 au that results from nonrectangular radial distribution of the asteroids. We fine-tuned the initial orbits of the giant planets in such a way that at the distance of 145 au, the radial density of the object equals approximately half of the radial density in the plateau region of the radial distribution. The border defined in this way can be easily controlled when the model with migration is applied, simply by shifting the initial positions of the planets, as most of the asteroids are being removed from the system shortly after the beginning of the simulation, when the giant planets are still close to their initial positions.

9. Discussion

Our results are derived under the major assumption that the orbital models of the HR 8799 systems are resonant, and the strong, zeroth Laplace MMR chain is likely the primary factor maintaining the long-term stability. However, some recent results in the literature might contradict this assumption, which possibly requires a comment.

Recently, Götberg et al. (2016) proposed long-term Lagrange-stable solutions found by tuning the initial orbital separations between the planets in terms of the Hill radii spacing (Chatterjee et al. 2008). These long-living models are reported as nonresonant, strongly chaotic, and prone to tiny changes of the initial conditions and a numerical scheme.

We examined system 94 (simulation 4e) in the Appendix of the source paper, given in the form of Cartesian astrocentric coordinates. The frequency analysis of this solution reveals that
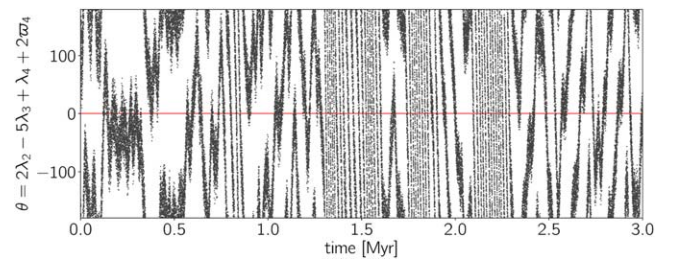

Figure 13. Temporal evolution of a critical argument θ of the three-body 2d:-5e:1b MMR of system 94, simulation 4e in Götberg et al. (2016; their Appendix). A sequence of alternating librations and rotations implies separatrix crossings and strongly chaotic evolution of the system.

it exhibits alternating rotations and librations of a critical argument of the three-body MMR 2d:-5c:1b (Figure 13). This feature indicates the separatrix crossing. We also did 2-dim $\langle Y \rangle$-scans in the (a_e, e_e) plane, close to this solution (not shown), which reveal a dense net of other narrow multibody MMRs in this region around $a_e \simeq 14.3$ au. The scans might be helpful to select other marginally stable solutions associated with narrow three- and four-body MMRs of higher orders.

The results of Götberg et al. (2016) are consistent with our simulations in the sense that they indicate a marginal stability of the system. It may be long-living only in very narrow stability regions in the phase space associated with various multibody MMRs. A resonance mechanism protecting the system from close encounters must be acting for the present planetary mass estimates, though the orbital evolution may be chaotic and marginally stable, as we also argue in Goździewski & Migaszewski (2009, 2014) and this work.

A determination of the Hill radii separation through semimajor axes expressed in the astrocentric reference frame

may be nonunique. For instance, the semimajor axis of HR 8799b in model 94 (simulation 4e) in Götberg et al. (2016) varies within 10 au, depending on the orbital phase, although the orbit has been initially set almost circular. It may be explained by indirect perturbations in the astrocentric frame; see Lee & Peale (2003) for details, as well as this work, regarding identification of MMRs in the outer debris disk (Sections 6 and 7). The osculating period of HR 8799b simultaneously varies between roughly 450 and 550 yr, hindering the proper identification of the MMRs. The identification is much easier in the canonical reference frame. In that frame, the N-body dynamics may be approximated to first order in the masses through the Keplerian orbits perturbed by the mutual interactions between the planets (e.g., Malhotra 1993).

A choice of the astrometric model is one more subtle, yet crucial factor for determining the long-term stable solutions. By reproducing the observations with Keplerian orbits, we dismiss information on the planet masses. Apparently, the mutual interactions should not be a significant factor for resolving the orbital geometry, given that the observed arcs are at most ~12% of the full orbits. However, the masses are critical for determining the dynamical interactions in the system; hence, skipping this prior seems to be inconsistent with the Bayesian inference. Even rigorously stable N-body models exhibit orbits that do not close after just one osculating period, due to fast precession (Section 3). Unstable models that are marginally worse from mathematically best-fitting solutions are unconstrained and represent widely open arcs during only one osculating period (Figure 6). These arguments indicate that the kinematic (geometric) models may already be biased, in spite of the short-arc measurements coverage.

10. Summary

In the first part of the paper, we present an updated astrometric model of the HR 8799 planetary system. If the masses of detected planets are in the range of a few Jupiter masses, the system is strongly unstable in a 1 Myr timescale. It is still a very short interval of time when compared to the star age, estimated to be between 30 and 160 Myr. Simulations of its dynamics conducted so far reveal that the long-term stable orbital architectures of the system must be confined to small and particular regions in the phase space. We attempt to solve this paradox by assuming that the HR 8799 system is involved in a two-body MMR chain or a multiple, three- or four-body MMR. Since the orbital parameters of a stable, resonant configuration are not independent and coupled, the number of free parameters of the astrometric model may be reduced to only five. This makes it possible to find stable solutions consistent with astrometric measurements and mass estimates derived from the planet formation and cooling theory.

While the original version of this optimization method was developed earlier, in this work, we propose a structured and CPU-efficient algorithm that consists of two independent steps. At the first stage, we build a database of stable configurations by simulating the planetary migration process. These synthetic, coplanar systems may agree only roughly with the spatial dimensions of the observed system. The second step performed with evolutionary algorithms is for fine-tuning these systems through linear scaling, rotations of the orbits in space, and propagating the bodies along their orbits with the N-body code

to the proper, observed positions. We note that during the latter step, the elements may change self-consistently, in accord with the N-body evolution.

This approach led us to finding the best-fitting model with $\chi^2_\nu \simeq 1$, which corresponds to the MMR chain of a generalized, four-body Laplace resonance. This solution to a subset of self-consistent astrometric measurements in Konopacky et al. (2016) extrapolates to all observations to date and preserves the correct timing. In particular, the extrapolated orbit of planet HR 8799d passes close to the first *HST* observation in 1998 (Lafrenière et al. 2009). Solutions unconstrained by the migration are widespread, in spite of much smaller $\chi^2_\nu \sim 0.74$, only marginally worse than the mathematically best-fitting configuration yielding $\chi^2_\nu \sim 0.6$. It may be a strong argument supporting our resonant model. Also, the mutual gravitational interactions between the planets are apparent, since the best-fitting N-body orbits may collide in a timescale of a few revolutions. That causes concern regarding kinematic models that do not account for the mutual interactions between the planets.

In the second part, we used the stable best-fitting initial conditions for simulating the dynamical structure of debris disks in the system. We developed CPU-efficient sampling of the initial conditions with the fast indicator MEGNO, dubbed the $\langle Y \rangle$-model. This dynamical model also makes it possible to locate additional, relatively massive objects in stable orbits, representing yet-undetected planets in the system. The HR 8799 system of four planets involved in the Laplace 8b:4c:2d:1e MMR is surprisingly robust for relatively strong perturbations introduced by such additional objects in the 1–$3\,m_{\rm Jup}$ range. Such unknown planets may be found interior or exterior to planets HR 8799e and HR 8799b, respectively, and extending the MMR chain to five or more planets.

With the $\langle Y \rangle$-model, we simulated the debris disks composed of small asteroids. The structure of these disks is represented by temporal coordinates in the orbital plane, as well as by the canonical Keplerian elements in the $(a_{\rm p}, e_{\rm p})$ plane. The simulations ended up with ~10^6 particles and revealed regions that may be populated by asteroids or small planets in stable orbits. The total number of tested initial conditions was 1–2 orders of magnitude larger when counting unstable solutions. The $\langle Y \rangle$-model was calibrated with the long-term, direct numerical integrations performed with the standard `Mercury 6.3` code. The results for the four- and five-planet restricted problems derived with the direct numerical integrations for 34–68 Myr closely overlap with outcomes from the $\langle Y \rangle$-model traced for much shorter intervals of 7–12 Myr.

The outer edge of the inner disk is shaped mostly by the inner planet e. A border of stable motions may be roughly determined by the collision zone with this planet. Close to its orbit, stable orbits are permitted only when asteroids or small-mass objects are trapped in low-order MMRs. The overall image of this zone is similar for a range of masses, between 10^{-15} (small asteroids) and $1\,m_{\rm Jup}$ (Jovian planets). By allowing for the initial eccentricities of the test bodies up to the limit determined by collisional orbits, we detected stable resonances, like 3:2 and 1:1 MMRs missing in earlier papers (Contro et al. 2016). The presence of a significant proportion of asteroids in these resonances may contribute to the highly nonsymmetric edge of the inner disk.

We also conducted CPU-intensive simulations of the outer disk, focusing on its inner edge and the inner part. Recently, it has been resolved with the ALMA observations in band 6

(1.34 mm) by Booth et al. (2016) and combined ALMA and VLA observations by Wilner et al. (2018). They found the inner edge at 145 ± 12 au and 104^{+8}_{-12} au, respectively. Extensive follow-up simulations by Read et al. (2018) focused on the fifth, undetected planet carving the outer disk, to be consistent with the model of Booth et al. (2016). Their best-fitting model predicts a small $0.1\,m_{\rm Jup}$ planet at $\simeq 138$ au. However, a different model in Wilner et al. (2018) may explain the ALMA and VLA observations with the currently observed four-body system. They also constrained a mass of planet HR 8799b to $5.8^{+7.9}_{-3.1}$ au.

We reconstructed the inner part of the disk composed of low-mass particles (asteroids) under different dynamical conditions covering scenarios in these three papers in the framework of the four- and five-planet restricted problem.

The inner edge is mostly influenced by the outermost planet. The simulations ended up with 10^6 bodies in stable orbits. The inner part of the outermost disk is spanned with various MMRs with this planet, including the 1:1 MMR and extended corotation zones. The width of these zones depends on the outermost planets' mass and may extend for ~ 100 au. A border of the stability region beyond the orbit of the outermost planet HR 8799b is determined by the collision zone with this planet. Low-order resonances, like the 4:3, 3:2, and 2:1 MMRs, force the eccentricity of the asteroids to moderate values. If these stable, moderate-eccentricity regions are populated, then the inner edge may exhibit a very complex shape. It turns out to be more asymmetric for smaller masses of the outermost planet. We found the most complex edge for $0.1\,m_{\rm Jup}$ at $\sim 138\,m_{\rm Jup}$, predicted in the best-fitting model to the ALMA observations in Read et al. (2018).

We note that in papers modeling the ALMA data, the edge is axisymmetric with inclusion of the Lagrangian clumps appearing as unimportant for the final results. However, our simulations indicate that the inner edge may be irregular, and particularly the 1:1 MMR zones overlapping with eccentric orbits in 3:2 and 4:3 MMRs may produce extended regions of emission. For instance, a $0.33\,m_{\rm Jup}$ planet placed at ~ 134 au would be responsible for maintaining two huge Lagrangian clumps spanning approximately 120×30 au each. A smaller planet of $\sim 0.1\,m_{\rm Jup}$ beyond ~ 135 au might permit a complex structure of stable motions interior to its orbit and confined to low-order MMRs with HR 8799b.

Finally, we tentatively simulated the migration of the four observed planets in the presence of an extended asteroidal belt. We assume that the planets migrate to the final state of the 8b:4c:2d:1e Laplace resonance and influence the asteroids. In this most complex astrophysical scenario, the disk edge may be moved to a "desired" location by appropriate migration rates and initial configuration of the planets. In such a case, no additional planets would be necessary in order to explain the ALMA observations. These simulations have a dynamic character, contrary to the static case considered in previous experiments. However, the static-type simulations made with the observed four-planet system are still complementary to the migration scenario. They reconstruct a detailed disk structure after the gaseous component has been dispersed and the planet migration has slowed down or stopped. In particular, they reveal the dynamical structure of less populated regions between ~ 90 and 150 au.

We conclude that the HR 8799 dynamical state cannot yet be fully resolved. While our resonant model may explain the astrometric observations, a longer time coverage is required to determine the real orbits without any doubt. As we confirm in this work, high-resolution images and observations of the debris disks may introduce additional, though indirect, limits on the HR 8799 system architecture. Various factors may be responsible for shaping the debris disks, like the presence of undetected planets and their masses and orbits. Therefore, interpretation of the SEDs and spatial disk imaging seems to be a complex and difficult problem, as the debris disk models may be nonunique. Our results and follow-up dynamical simulations similar to those made in our paper could be helpful to reduce this indeterminacy.

ORCID iDs

Krzysztof Goździewski ⓘ https://orcid.org/0000-0002-8705-1577

References

Adachi, I., Hayashi, C., & Nakazawa, K. 1976, PThPh, 56, 1756
Armitage, P. J. 2018, arXiv:1803.10526
Baines, E. K., White, R. J., Huber, D., et al. 2012, ApJ, 761, 57
Baraffe, I., Chabrier, G., Barman, T. S., Allard, F., & Hauschildt, P. H. 2003, A&A, 402, 701
Beaugé, C., Michtchenko, T. A., & Ferraz-Mello, S. 2006, MNRAS, 365, 1160
Bergfors, C., Brandner, W., Janson, M., Köhler, R., & Henning, T. 2011, A&A, 528, A134
Bevington, P. R., & Robinson, D. K. 2003, Data Reduction and Error Analysis for the Physical Sciences (Boston: McGraw-Hill)
Booth, M., Jordán, A., Casassus, S., et al. 2016, MNRAS, 460, L10
Chambers, J. E. 1999, MNRAS, 304, 793
Chambers, J. E., Wetherill, G. W., & Boss, A. P. 1996, Icar, 119, 261
Charbonneau, P. 1995, ApJS, 101, 309
Chatterjee, S., Ford, E. B., Matsumura, S., & Rasio, F. A. 2008, ApJ, 686, 580
Cincotta, P. M., Giordano, C. M., & Simó, C. 2003, PhyD, 182, 151
Cincotta, P. M., & Simó, C. 2000, A&AS, 147, 205
Contro, B., Horner, J., Wittenmyer, R. A., Marshall, J. P., & Hinse, T. C. 2016, MNRAS, 463, 191
Currie, T. 2016, arXiv:1607.03980
Currie, T., Burrows, A., Itoh, Y., et al. 2011, ApJ, 729, 128
Currie, T., Fukagawa, M., Thalmann, C., Matsumura, S., & Plavchan, P. 2012, ApJL, 755, L34
de Souza Torres, K., & Anderson, D. R. 2008, arXiv:0808.0483
Esposito, S., Mesa, D., Skemer, A., et al. 2013, A&A, 549, A52
Fabrycky, D. C., & Murray-Clay, R. A. 2010, ApJ, 710, 1408
Foreman-Mackey, D., Hogg, D. W., Lang, D., & Goodman, J. 2013, PASP, 125, 306
Gaia Collaboration, Brown, A. G. A., Vallenari, A., et al. 2018, A&A, 616, A1
Galicher, R., Marois, C., Macintosh, B., Barman, T., & Konopacky, Q. 2011, ApJL, 739, L41
Götberg, Y., Davies, M. B., Mustill, A. J., Johansen, A., & Church, R. P. 2016, A&A, 592, A147
Goździewski, K., Breiter, S., & Borczyk, W. 2008, MNRAS, 383, 989
Goździewski, K., & Migaszewski, C. 2009, MNRAS, 397, L16
Goździewski, K., & Migaszewski, C. 2014, MNRAS, 440, 3140
Hadden, S., & Lithwick, Y. 2018, AJ, in press (arXiv:1803.08510)
Hairer, E., Wanner, G., & Lubich, L. 2002, Geometric Numerical Integration: Structure-Preserving Algorithms for Ordinary Differential Equations (2nd ed.; Berlin: Springer)

Hinkley, S., Carpenter, J. M., Ireland, M. J., & Kraus, A. L. 2011, ApJL, 730, L21
Hinz, P. M., Rodigas, T. J., Kenworthy, M. A., et al. 2010, ApJ, 716, 417
Izzo, D., Ruciński, M., & Biscani, F. 2012, in The Generalized Island Model, Vol. 415 (Berlin: Springer), 151
Konopacky, Q. M., Marois, C., Macintosh, B. A., et al. 2016, AJ, 152, 28
Lafrenière, D., Marois, C., Doyon, R., & Barman, T. 2009, ApJL, 694, L148
Laskar, J. 1993, CeMDA, 56, 191
Laskar, J., & Robutel, P. 2001, CeMDA, 80, 39
Lee, M. H., & Peale, S. J. 2003, ApJ, 592, 1201
Maire, A. L., Skemer, A. J., Hinz, P. M., et al. 2015, A&A, 579, 2
Malhotra, R. 1993, ApJ, 407, 266
Malhotra, R. 1998, in ASP Conf. Ser. 149, Solar System Formation and Evolution, ed. D. Lazzaro et al. (San Francisco, CA: ASP), 37
Marleau, G.-D., & Cumming, A. 2014, MNRAS, 437, 1378
Marois, C., Macintosh, B., Barman, T., et al. 2008, Sci, 322, 1348
Marois, C., Zuckerman, B., Konopacky, Q. M., Macintosh, B., & Barman, T. 2010, Natur, 468, 1080
Marshall, J., Horner, J., & Carter, A. 2010, IJAsB, 9, 259
Matthews, B., Kennedy, G., Sibthorpe, B., et al. 2014, ApJ, 780, 97
Metchev, S., Marois, C., & Zuckerman, B. 2009, ApJL, 705, L204
Moore, A., Hasan, I., & Quillen, A. C. 2013, MNRAS, 432, 1196
Morbidelli, A. 2002, Modern Celestial Mechanics: Aspects of Solar System Dynamics (Boca Raton, FL: CRC Press)
Moro-Martín, A., Malhotra, R., Bryden, G., et al. 2010, ApJ, 717, 1123

Morrison, S. J., & Kratter, K. M. 2016, ApJ, 823, 118
Oppenheimer, B. R., Baranec, C., Beichman, C., et al. 2013, ApJ, 768, 24
Panichi, F., Goździewski, K., & Turchetti, G. 2017, MNRAS, 468, 469
Papaloizou, J. C. B. 2015, IJAsB, 14, 291
Papaloizou, J. C. B., & Terquem, C. 2006, RPPh, 69, 119
Price, K., Storn, R. M., & Lampinen, J. A. 2005, Differential Evolution: A Practical Approach to Global Optimization (Berlin: Springer)
Pueyo, L., Soummer, R., Hoffmann, J., et al. 2015, ApJ, 803, 31
Read, M. J., Wyatt, M. C., Marino, S., & Kennedy, G. M. 2018, MNRAS, 475, 4953
Reidemeister, M., Krivov, A. V., Schmidt, T. O. B., et al. 2009, A&A, 503, 247
Šidlichovský, M., & Nesvorný, D. 1996, CeMDA, 65, 137
Skemer, A. J., Hinz, P. M., Esposito, S., et al. 2012, ApJ, 753, 14
Sokal, A. D. 1996, Lectures at the Cargése Summer School on Functional Integration: Basics and Applications, Vol. 76, http://www.stat.unc.edu/faculty/cji/Sokal.pdf
Soummer, R., Brendan Hagan, J., Pueyo, L., et al. 2011, ApJ, 741, 55
Su, K. Y. L., Rieke, G. H., Stapelfeldt, K. R., et al. 2009, ApJ, 705, 314
Sudol, J. J., & Haghighipour, N. 2012, ApJ, 755, 38
van Leeuwen, F., & Fantino, E. 2005, A&A, 439, 791
Wertz, O., Absil, O., Gómez González, C. A., et al. 2017, A&A, 598, A83
Wilner, D. J., MacGregor, M. A., Andrews, S. M., et al. 2018, ApJ, 855, 56
Zurlo, A., Vigan, A., Galicher, R., et al. 2016, A&A, 587, A57